Thermoelectric Properties of 2,7-Dipyridylfluorene Derivatives in Single-Molecule Junctions

Gilles Yzambart,[†,∃] Laura Rincón-García,[‡,§,∃] Alaa A. Al-Jobory,[‖,⊥,∃] Ali K. Ismael, [‖,#,∃] Gabino Rubio-Bollinger,[‡,○] Colin J. Lambert,*[,‖] Nicolás Agraït,* [‡,§,○] Martin R. Bryce*[,†]

[†] Department of Chemistry, Durham University, Durham DH1 3LE, UK

[‡] Departamento de Física de la Materia Condensada, Universidad Autónoma de Madrid, E-28049 Madrid, Spain

[§] Instituto Madrileño de Estudios Avanzados en Nanociencia IMDEA-Nanociencia, E-28049 Madrid, Spain

[‖] Department of Physics, Lancaster University, Lancaster LA1 4YB, UK

[⊥] Department of Physics, College of Education for Pure Science, University of Anbar, Anbar, Iraq

[#] Department of Physics, College of Education for Pure Science, Tikrit University, Tikrit, Iraq

[○] Condensed Matter Physics Center (IFIMAC) and Instituto Universitario de Ciencia de Materiales "Nicolás Cabrera" (INC), Universidad Autónoma de Madrid, E-28049 Madrid, Spain

[∃] These Authors contributed equally to this work.

ABSTRACT

A series of 2,7-dipyridylfluorene derivatives has been synthesized with different substituents (2H, 2Me, 2OMe, $2CF_3$ and O) at the C(9) position. Experimental measurements on gold|single-molecule|gold junctions, using a modified scanning tunneling microscope-break junction (STM-BJ) technique show that the C(9) substituent has little effect on the conductance, although there is a more significant influence on the thermopower, with the Seebeck coefficient varying by a factor of 1.65 within the series. The combined experimental and computational study, using density functional theory (DFT) calculations, provides insights into the interplay of conductance and thermopower in single-molecule junctions and is a guide for new strategies for thermopower modulation in single-molecule junctions.

INTRODUCTION

The measurement, control and understanding of charge transport through single molecules is of fundamental interest and is central to the development of molecular electronic devices.[1-3] A new direction for this field of research has emerged with the recent advances in techniques to measure the thermoelectric properties of organic molecules connected in electrode|single-molecule|electrode junctions.[4] This topic is providing new chemical and physical insights into charge transport at the single-molecule level. Devices with a high thermoelectric efficiency could have future applications in thermal management and the conversion of waste heat into electricity in energy harvesting applications, or for on-chip cooling in electronic devices. Molecular junctions may also be cheaper to produce and be more environmentally friendly than the present inorganic semiconducting thermoelectric devices.[5-7]

Combined experimental and theoretical studies have demonstrated that the thermopower, or Seebeck coefficient *S*, of a single-molecule junction is dependent upon chemical composition and the position of the molecular energy levels with respect to the Fermi level of the metal electrodes.[8] Examples of organic molecules used in these studies include fullerenes,[9-12] benzenedithiol,[9, 11, 13] oligothiophenes with thiolate end-groups,[14] and molecules with amine or pyridyl anchors, namely 1,4-diaminobenzene and π–extended analogs, and 4,4'-bipyridine.[15] Thermopower studies have addressed such factors as: substituent effects on a phenyl core and variation of the anchor group,[16] dependence on molecular length,[14,15,17] the comparison of conjugated versus non-conjugated bridging units,[14] dependence on energy alignment in the junction,[18] and quantum interference effects in the molecular backbone.[19]

The present work investigates a series of five fluorene (Fl)-based molecules **1**–**5** whose structures are shown in **Figure 1**. The motivation is to study the influence on transport properties in gold|single-molecule|gold junctions of different side-groups on the same backbone. All the molecules have terminal pyridyl anchoring units at both ends, and they differ only in the substituents at C(9), namely 2H, 2Me, 2OMe, $2CF_3$ and O (molecules **1-5**, respectively). Fluorene is a planarized biphenyl system and it was chosen as the backbone for three reasons: (i) it is an established unit in single-molecule conductance studies using break-junction techniques[20-24] although it has not been studied previously in thermopower measurements; (ii) the substituents at C(9) can be systematically varied by chemical substitution to attach electron-donating (Me or OMe) or electron-withdrawing (CF_3) groups; (iii) the C(9) carbon is sp^3 hybridized in compounds **1-4**, so the substituents in these molecules are not directly conjugated to the π–system of the backbone. The effects of non-conjugated pendant substituents on thermopower has not, to our knowledge, been studied previously. Fluorenone compound **5** is

electronically different from **1-4** as the pendant oxygen atom of **5** is conjugated to the backbone through the sp^2-hybridized carbon. A modified STM-BJ technique, combined with DFT calculations, has provided an in-depth analysis of the transport mechanisms in compounds **1-5**. The results show that the different substituents affect the thermopower, but have a negligible influence on the conductance of the molecular junctions.

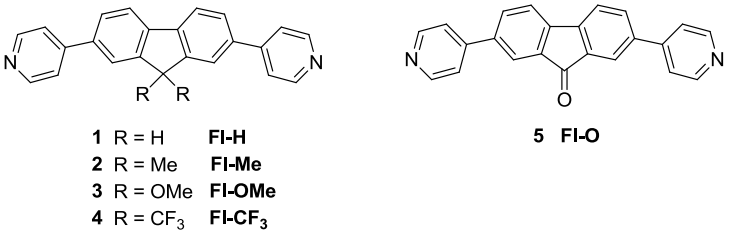

1 R = H **Fl-H**
2 R = Me **Fl-Me**
3 R = OMe **Fl-OMe**
4 R = CF_3 **Fl-CF_3**

5 **Fl-O**

Figure 1. Structures of the molecules studied in this work

EXPERIMENTAL SECTION

Molecular Synthesis. Compounds **1**[25] and **5**[26] were synthesized as reported previously. The new fluorene derivatives **2-4** were synthesized in 55-67% yields from the corresponding dihalo precursors by two-fold Suzuki-Miyaura reactions with 4-pyridylboronic acid. Full details of the synthesis and spectroscopic characterization are given in the Supporting Information. 2,7-Dibromo-9,9-dimethylfluorene was obtained commercially from Sigma-Aldrich. 2,7-Dibromo-9,9-dimethoxyfluorene was obtained in 98% yield by reaction of 2,7-dibromofluorenone with trimethylorthoformate in a refluxing mixture of concentrated sulfuric acid and methanol. The synthesis of the bis(trifluoromethyl) derivative **4** was more challenging and is shown in **Scheme 1**. The intermediate **C** was synthesized by a new route which is practically considerably more convenient (although lower yielding) than the literature procedure in which the CF_3 groups were derived from gaseous hexafluoracetone.[27] Our route from **A** to **B** uses the protocol for the synthesis of 1,1,1,3,3,3-hexafluoro-2-organyl-propan-2-ol, in which the CF_3 groups are

introduced using trifluorotrimethylsilane (Ruppert's reagent).[28] Dehydration of **B** yielded **C** which was then iodinated to **D** as reported.[27] Finally, the palladium-catalyzed reaction of **D** with 4-pyridylboronic acid gave the target product **4**.

Scheme 1. Synthetic route to molecule **4**

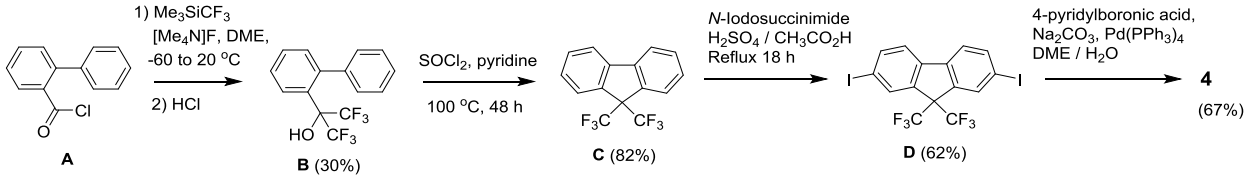

Sample preparation. The compounds **1-5** were each deposited by drop-casting onto a 250 nm thick annealed Au(111) film on glass substrates (Arrandee^{TM}, Germany). Before deposition, the Au surface was annealed at a temperature above 900 K for less than 1 minute in order to have a clean polycrystalline surface (see Figure S24 in Supporting Information). After cooling down to room temperature, the Au substrates were immersed in a 1 mM solution of **1-5** in dichloromethane (DCM) for 30 min and then dried with streaming nitrogen. The coverage of the substrate is well below that of the monolayer and areas can be found without molecules where junction formation is not observed.

Scanning tunneling microscopy (STM). STM measurements were performed using a home-built STM modified to measure simultaneously the conductance G and thermopower S of single-molecule junctions.[10] Mechanically cut Au tips (0.25 mm diameter, 99.99% purity, Goodfellow) were used to contact the molecules and STM-BJ measurements were performed in ambient conditions and at room temperature, with a bias voltage V_{bias} applied to the substrate. Single-molecule junctions were formed after breaking the Au-Au contact formed by indenting the

substrate with the STM tip. The experimental technique is described in more detail in the Supporting Information.

A 1 kΩ resistor mounted in the tip support was used as a heater to establish a temperature difference ΔT between the substrate (at room temperature, T_c) and the tip (heated at a temperature $T_h > T_c$). Thermoelectric properties of each molecule were measured by applying four different ΔTs, namely $\Delta T = T_h - T_c = 0\ K$, $\sim 15\ K$, $\sim 22\ K$ and $\sim 30\ K$, monitored with thermocouples in the resistor and substrate. For each ΔT, the system was allowed to stabilize for approximately 20 min before measurements were taken.

The thermopower S of single-molecule junctions was measured during the breaking of the junction, stopping the tip motion every 40-60 pm, as described in Figure S25 in the Supporting Information. The bias voltage was maintained at a fixed value $\Delta V = V_{bias} = 200$ mV during the tip motion and it was swept twice every few picometers between $\pm\Delta V_0 = \pm 10$ mV while the tip was stationary. Current-voltage (*I-V*) curves show a voltage offset when measuring in the presence of a temperature difference ΔT between the two Au electrodes. This voltage offset is related to the thermovoltage V_{th} of the junction (see Supporting Information). Knowing also the temperature difference ΔT, the thermopower or Seebeck coefficient S of the junction was calculated using the following equation (1):

$$S = -\frac{V_{th}}{\Delta T} \quad (1)$$

Experiments were performed at zero ΔT and at three different ΔT values for each molecule to ensure a good linear fit of all the V_{th} values and equation 1 was used to calculate the thermopower S. The conductance is measured both from the current values while moving the tip ($V_{bias} = 200$ mV) and from the slope of the *I-V* curves.

Computational Details. Electronic structure calculations were performed using the DFT code SIESTA.[29] The optimum geometries of the isolated molecules were obtained by relaxing the molecules until all forces on the atoms were less than 0.05 eV/Å. The SIESTA calculations employed a double-zeta plus polarization orbital basis set and norm-conserving pseudopotentials; an energy cutoff of 250 Rydbergs defined the real space grid and the exchange correlation functional was LDA. To calculate their electrical conductance, the molecules were attached to gold leads via the pyridyl anchor groups. The leads were constructed of 6 layers of Au(111) each containing 30 gold atoms and the optimum binding distance was calculated to be 2.4 Å (Figure S3 in Supporting Information) between the terminal nitrogen atoms and a 'top' gold atom. A Hamiltonian describing this structure was produced using SIESTA and the zero-bias transmission coefficient $T(E)$ was calculated using the Gollum code.[30] Further details are provided in the Supporting Information.

It is well known that DFT frequently underestimates the HOMO-LUMO gap[31,32] and from Table S1 in the Supporting Information it is clear that the calculated gaps are less than the optically-measured gaps. To overcome this deficiency, a scissor correction is performed by diagonalizing the molecular sub-matrix of the full Hamiltonian, then shifting the eigenvalues below and above the Fermi energy such that the new HOMO-LUMO gap matches the experimental value of the isolated molecule. Finally, the diagonalized matrix is transformed back to the original basis to obtain the corrected full Hamiltonian.

RESULTS AND DISCUSSION

In order to find the most probable value of the conductance of each molecule $\bar{G}$, 1D histograms were plotted with all the conductance values obtained from each junction break (**Figure 2**). A peak can be identified in the histograms corresponding to the Au-Au contact (at $G = G_0$, where

G_0 is the quantum of conductance, $G_0 = 2e^2/h$). The values on the left of the histograms correspond to the noise level of the system, below $10^{-6.5}\ G_0$. An extra peak, not present when measuring only Au-Au contacts, is observed that corresponds to the molecular junction formation. While the tip is retracting from the surface, a molecule may connect both electrodes. As the tip separates further from the surface the conductance remains almost constant resulting in a conductance plateau in the conductance G vs displacement Δz curves, instead of decreasing exponentially, as occurs with Au-Au tunneling. Figure S26 in Supporting Information shows the 2D histograms for each molecule built from the G vs Δz curves. These plateaus create a junction-characteristic peak in the G 1D histograms. Using a Gaussian fit, $\bar{G}$ (the expected value) and σ_G, the standard deviation, are obtained.

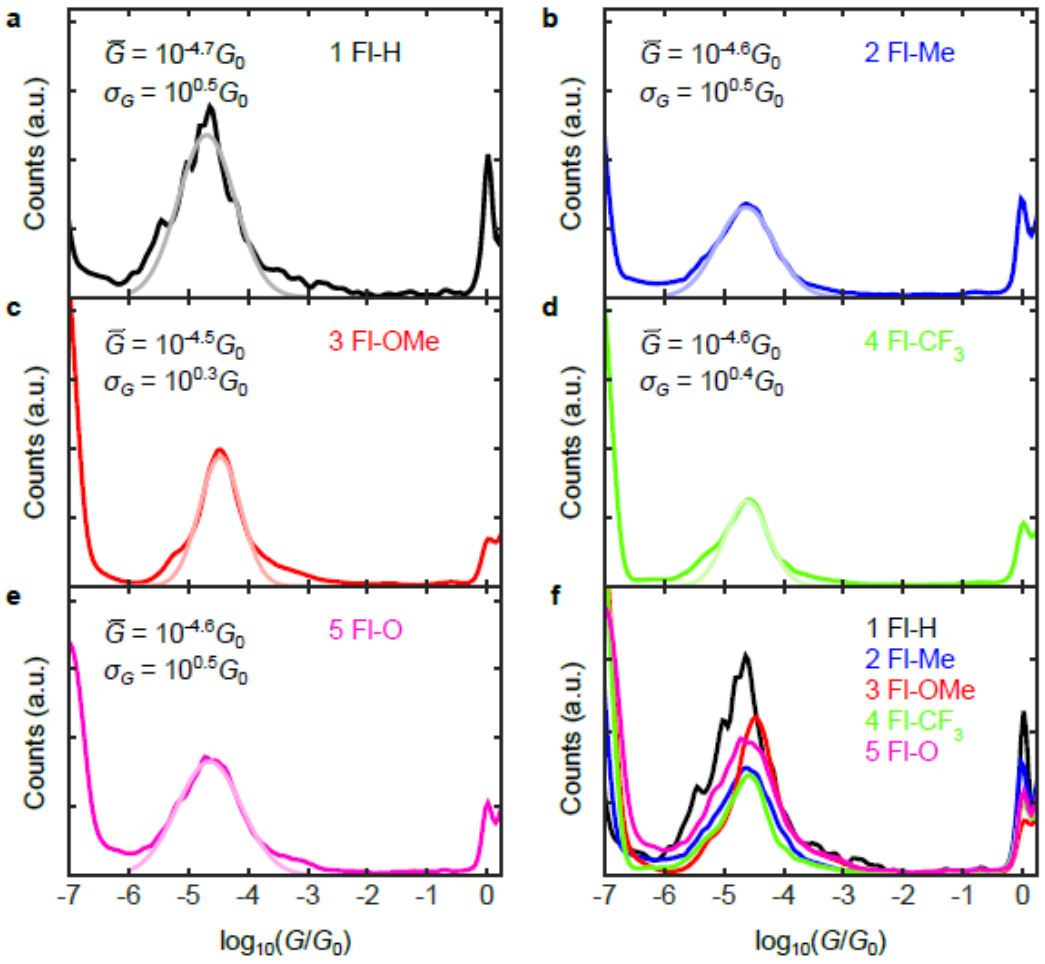

Figure 2. Conductance G 1D histograms. a-e) Conductance G 1D histogram of each molecule and Gaussian fit of the peak corresponding to the junction values, plotted in a lighter color superimposed to the histograms. $\bar{G}$ and σ_G in each panel are the expected value (most probable value) of the conductance and the standard deviation of the fit, respectively. f) Conductance G 1D histograms of all the molecules. Each histogram is normalized with its total number of measured values.

A very similar conductance value was obtained for each of molecules **1-5**, as a consequence of the similar transport pathways in each molecule, which are located predominantly on the conjugated backbone. The data are shown in **Figure 2** and summarized in **Table 1**. The values we report are similar to those previously reported for other fluorene derivatives with thiol anchor groups, using different break-junction techniques.[21, 22]

Table 1. Measured conductances (column 2), conductance histogram widths (column 3) and Seebeck coefficients (column 4).

Molecule	$\log_{10}(\bar{G}/G_0)$	**Standard deviation** $\log_{10}(\sigma_G/G_0)$	$\bar{S}\ (\mu V/K)$
1 Fl-H	-4.7	0.5	-5.5
2 Fl-Me	-4.6	0.5	-8.6
3 Fl-OMe	-4.5	0.3	-7.4
4 Fl-CF_3	-4.6	0.4	-8.0
5 Fl-O	-4.6	0.5	-9.0

To study the thermoelectric properties of the Au|molecule|Au junctions, the thermovoltage V_{th} was measured while the junction breaks using four temperature differences between tip and sample, namely $\Delta T = 0\,K$, $\sim 15\,K$, $\sim 22\,K$ and $\sim 30\,K$. **Figure 3a** shows the equivalent thermal circuit taking into account the contribution from the lead connecting the heated tip (see further details in the Supporting Information). More than one set of measurements

was carried out for each ΔT and each molecule. **Figure 3** shows a plot of V_{th} 1D histograms with the values of all the sets of measurements at each ΔT and the fit to a Gaussian distribution (plotted in a lighter color superimposed on the histograms in **Figure 3**).

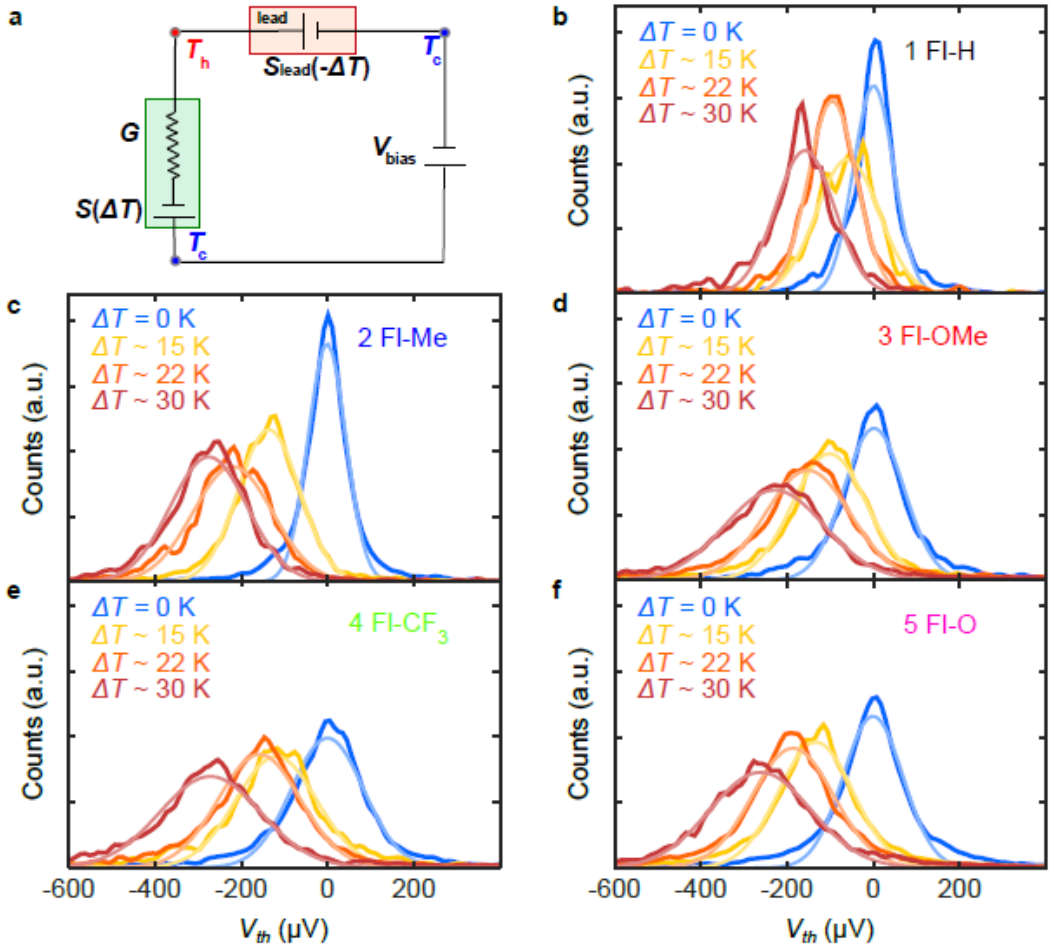

Figure 3. Thermal circuit and thermovoltage V_{th} 1D histograms for compounds **1-5**. a) Equivalent thermal circuit. Besides the thermovoltage produced in the molecular junction, there is another contribution from the lead that connects the heated tip, equal to $S_{lead}(-\Delta T)$, where S_{lead} is the thermopower of the lead (see further details in the Supporting Information). b-f) Thermovoltage V_{th} 1D histograms of each molecule and Gaussian fits, plotted in a lighter color superimposed on the histograms.

Figure 4 shows the mean value $\overline{V_{th}}$ of each set of measurements as a function of the temperature difference ΔT (empty circles). The error bars of $\overline{V_{th}}$ are the standard deviations $\sigma_{V_{th}}$ obtained from the Gaussian fit of each set of measurements. The linear fit shown in **Figure 4** is obtained by fitting all the individual V_{th} values independently, without taking into account if one set of measurements has more or less points than another. The slope of this fit corresponds to the thermopower S of the molecule and the values are shown as an inset in each plot. The relative error of S obtained with this fit is smaller than 2% in all cases, meaning that there are sufficient measurements to give a reliable value of S.

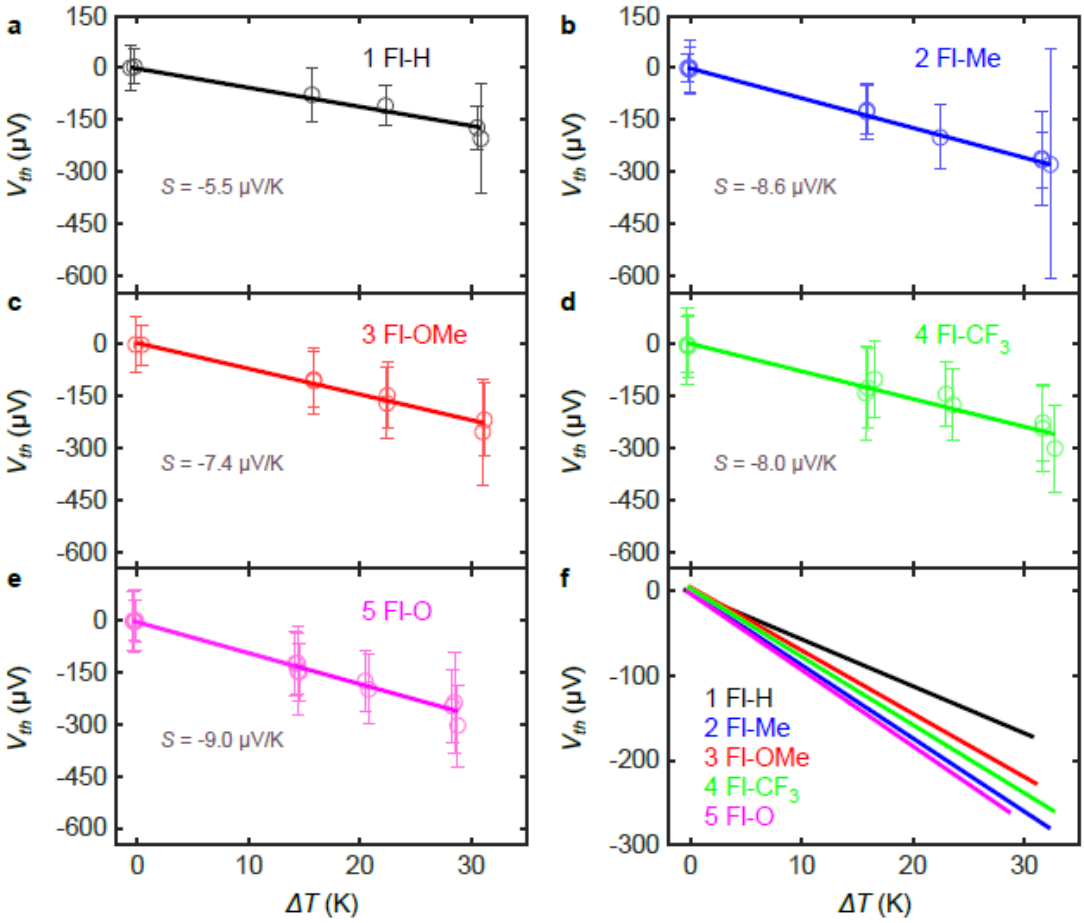

Figure 4. Thermopower S values. a-e) Linear fit to all the V_{th} values for molecules **1-5**, respectively, to obtain the thermopower S of each molecule, which is the slope of this fit (values are shown in each plot). The empty circles correspond to the mean thermovoltage value $\overline{V_{th}}$

obtained from the Gaussian fit of each set of measurements. The error bars of $\overline{V_{th}}$ are the standard deviations $\sigma_{V_{th}}$and are typically between $73\,\mu V$ for $\Delta T = 0\,K$ to $135\,\mu V$ for $\Delta T \sim 30\,K$ (as can be seen in the figure). f) Linear fit of all the V_{th} values shown in panels a-e, combined for comparison.

The Seebeck coefficients of the different molecules are summarized in Table 1, with a variation from $-5.5\,\mu V/K$ in the lowest case (compound **1**) to $-9.0\,\mu V/K$, in the highest case (compound **5**). The experimental results show that the variation of the C(9) substituents has little effect on the conductance, while having a more significant effect on the thermopower, increasing the Seebeck coefficient by a factor of 1.65. The data show that all the substituents at C(9) slightly increase the thermopower (compared to the unsubstituted molecule **1**) and the values for **2-5** do not follow a trend in the electron-donating or electron-withdrawing effect of the substituent. The sign of *S* for all the compounds **1-5** is negative, consistent with the Fermi level being closer to the lowest unoccupied molecular orbital (LUMO) than to the highest occupied molecular orbital (HOMO).[4]

Figure 5 shows the DFT-predicted transmission coefficients for the molecules, as a function of E-E_M , where E_M is the energy of the middle of the HOMO-LUMO gap. Note that the slope of $T(E)$ near the mid-gap is not zero, because $T(E)$ is rather asymmetric within the gap. This asymmetry arises because the HOMOs of these molecules are degenerate, as shown in Figures S4 – S8 in the SI. Indeed, as described by the Breit-Wigner formula[33] when on-resonance the transmission coefficient of a symmetric molecule should be unity, unless the resonant level is degenerate. This is why the HOMO transmission resonances in Figure 5 are much less than unity, whereas the non-degenerate LUMO resonances are close to unity. There is no frontier orbital distribution on the pendant group at C(9) for molecules **1-4** (Figures S4-S7)

whereas for molecule **5** there is a contribution of the HOMO, LUMO and LUMO+1 on the fluorenone oxygen atom (Figure S8). Nevertheless, in common with those of **1-4**, the orbitals of **5** are predominantly located on the backbone and as shown in Figure 5, the transmission function of **5** is almost identical with those of **1-4** within the HOMO-LUMO gap. This explains the similar experimental results for the conductance of **1-5**. The transmission function $T(E)$ includes the effect of contacts and unlike the electrical conductance (which is obtained by thermally averaging $T(E)$) does not depend on temperature. Therefore, a low temperature measurement is unlikely to reveal further differences between the molecules.

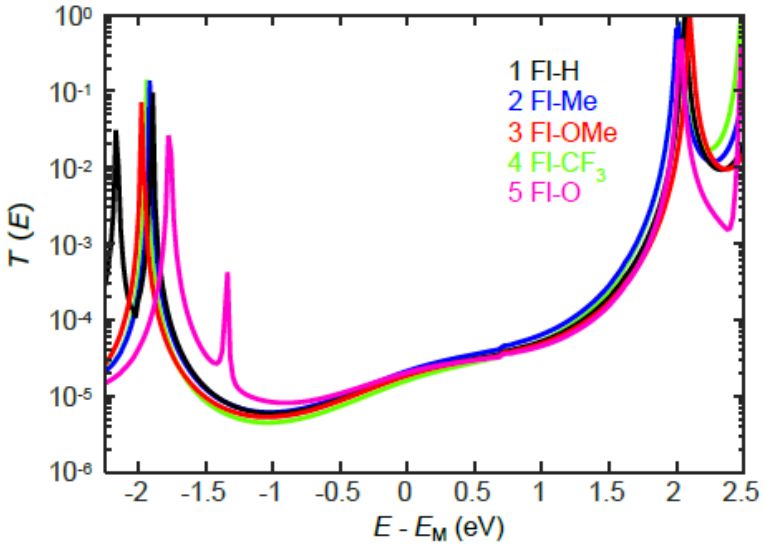

Figure 5. Transmission coefficients $T(E)$ for molecules **1-5** after scissor corrections.

Figure 6 shows a comparison between the theoretical conductances and Seebeck coefficients obtained from the transmission curves. In agreement with experiment, the Seebeck coefficient is negative, due to the presence of the pyridyl anchors, which tend to move the LUMO towards the Fermi energy. Since the Fermi energy is determined in part by environmental factors, theoretical results are shown for two values of the Fermi energy, namely $E_F=E_M$ and $E_F=E_M$-0.3 eV. This window captures the experimental values of both conductance and thermopower. The differences between experiment and theory most likely arise from the fact that the Fermi energy (relative to frontier orbital energies) varies from molecule to molecule.

Table 2 shows that almost exact agreement between theory and experiment can be obtained if small variations in E_F occur between the molecules.

Table 2. Theoretical results obtained using the Fermi energies shown in column 2.

Molecule	E_F-E_M **(eV)**	**Exp.** $\overline{S}$ **(μV/K)**	**Theo.** $\overline{S}$ **(μV/K)**	**Exp.** $\log_{10}(\overline{G}/G_0)$	**Theo.** $\log_{10}(\overline{G}/G_0)$
1 Fl-H	0.40	-5.5	-6.8	-4.7	-4.6
2 Fl-Me	0.10	-8.6	-8.6	-4.6	-4.6
3 Fl-OMe	0.16	-7.4	-7.4	-4.5	-4.6
4 Fl-CF_3	0.10	-8.0	-8.1	-4.6	-4.6
5 Fl-O	-0.15	-9.0	-9.1	-4.6	-4.7

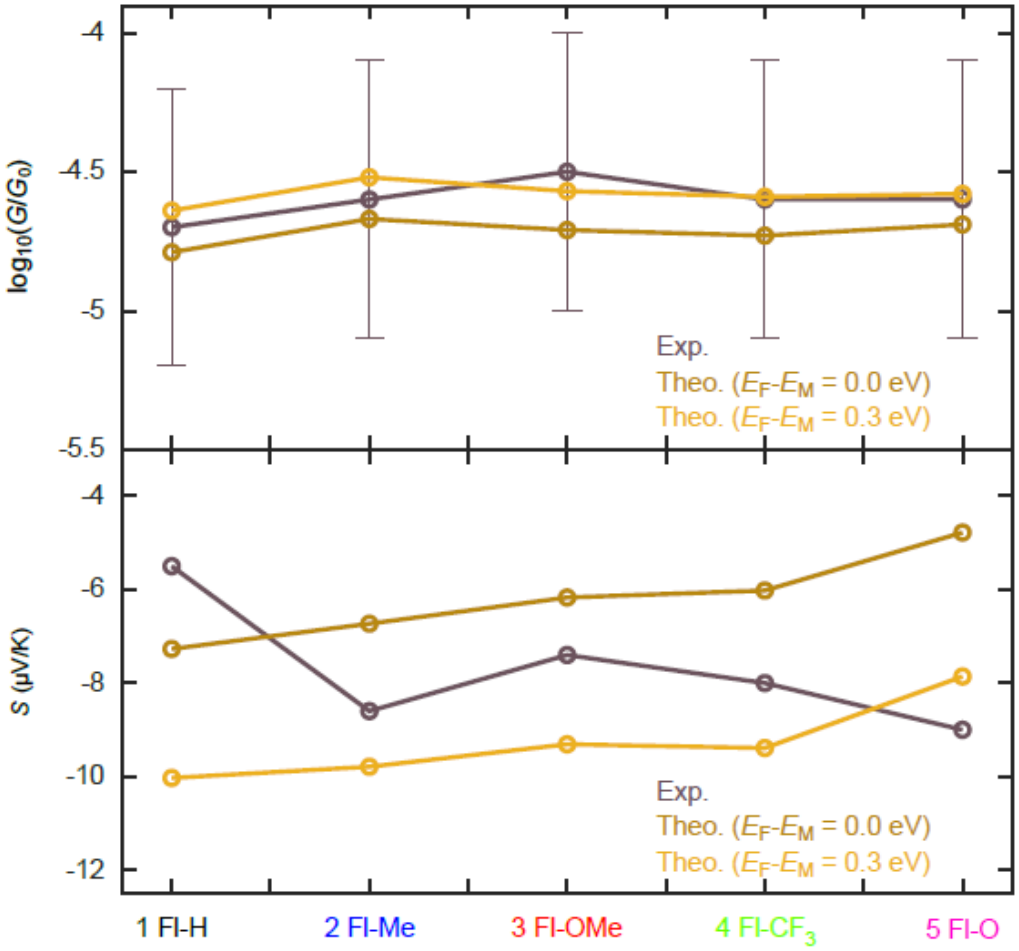

Figure 6. Conductance and Seebeck theoretical and experimental results. Top panel: a comparison between measurements and calculations of conductance. The error bars correspond to the standard deviation shown in Table 1. Bottom panel: a comparison between measurements and calculations of Seebeck coefficients

CONCLUSIONS

A series of fluorene derivatives **1-5** has been synthesized and their conductance and thermopower have been measured in gold|single-molecule|gold junctions using a modified STM-BJ technique. By systematically varying the pendant group, the Seebeck coefficient can be varied from -5.5 μV/K for molecule **1** to -9 μV/K for molecule **5** which is an increase of almost 80%, whereas the electrical conductance remains essentially unchanged across the series of molecules. This combined experimental and computational study demonstrates that fluorene is a suitable backbone unit for measurements of thermopower, and that non-conjugated pendant substituents can influence the thermopower of a molecular system – a topic that has not been studied previously. Future strategies could be to attach substituents at different positions on the fluorene ring for thermopower enhancement in single-molecule junctions, and for studying quantum interference effects through a fluorene backbone.

ASSOCIATED CONTENT

Supporting Information. The Supporting Information is available free of charge on the ACS Publications website at DOI:xxxxxxxxx

Synthesis and characterization details of the new molecules; methods and results for the single-molecule conductance and thermopower measurements for compounds **1-5**; computational methods and data (PDF).

AUTHOR INFORMATION

Corresponding Authors

*E-Mail: c.lambert@lancaster.ac.uk

*E-Mail: nicolas.agrait@uam.es

*E-Mail: m.r.bryce@durham.ac.uk

Author Contributions

The manuscript was written with contributions of all authors. All authors have given approval to the final version of the manuscript. G.Y., L.R.-G., A.A.A. and A.K.I. contributed equally to this work.

Acknowledgements

This work was supported by the EC FP7 ITN Grant no. 606728 "MOLESCO" and the EC H2020 FET Open project 767187 "QuIET". Equipment in Durham was funded by EPSRC grant EP/L02621X/1. The work in Lancaster was supported by the EPSRC "QuEEN" programme grant EP/N017188/1. Further support from the UK EPSRC is acknowledged, through grants EP/M014452/1, EP/P027156/1 and EP/N03337X/1. N.A. and G.R.-B. acknowledge the Spanish MINECO (grants MAT2014-57915-R, MAT2017-88693-R and MDM-2014-0377) and

Comunidad de Madrid (grant NANOFRONTMAG-CM, S2013/MIT-2850). L.R.-G. acknowledges financial support from the Spanish MECD (grant no. FPU14/03368). Funding is acknowledged from the Iraqi Ministry of Higher Education (SL-20). A.K.I. acknowledges financial support from Tikrit University (Iraq). A.A.A. acknowledges financial support from University of Anbar (Iraq).

Notes

The authors declare no competing financial interest.

REFERENCES

(1) Cuevas, J. C.; Scheer, E. *Molecular Electronics: An Introduction to Theory and Experiment*; World Scientific Publishing Co. Pte. Ltd.: Singapore, 2010.

(2) Xiang, D. Molecular-Scale Electronics: From Concept to Function. *Chem. Rev.* **2016**, *116*, 4318–4440.

(3) Leary, E.; La Rosa, A.; M. González, M. T.; Rubio-Bollinger, G.; Agraït, N.; Martın, N. Incorporating Single Molecules into Electrical Circuits. The Role of the Chemical Anchoring Group. *Chem. Soc. Rev.* **2015**, *44*, 920–942.

(4) Rincon-Garcia, L.; Evangeli, C.; Rubio-Bollinger, G.; Agraït, N. Thermopower Measurements in Molecular Junctions. *Chem. Soc. Rev.* **2016**, *45*, 4285–4306.

(5) Malen, J. A.; Yee, S. K.; Majumdar, A.; Segalman, R. A. Fundamentals of Energy Transport, Energy Conversion and Thermal Properties in Organic-Inorganic Heterojunctions. *Chem. Phys. Lett.* **2010**, *491*, 109−122.

(6) Zhang, Q.; Sun, Y.; Xu, W.; Zhu, D. Organic Thermoelectric Materials: Emerging Green Energy Materials Converting Heat to Electricity Directly and Efficiently. *Adv. Mater.* **2014**, *26*, 6829–6851.

(7) Dubi, Y.; Di Ventra, M. Colloquium: Heat Flow and Thermoelectricity in Atomic and Molecular Junctions. *Rev. Mod. Phys.* **2011**, *83*, 131−155.

(8) Baheti, K.; Malen, J. A.; Doak, P.; Reddy, P.; Jang, S-Y.; Tilley, T. D.; Majumdar, A.; Segalman, R. A. Probing the Chemistry of Molecular Heterojunctions Using Thermoelectricity. *Nano Lett.* **2008**, *8*, 715–719.

(9) Yee, S. K.; Malen, J. A.; Majumdar, A.; Segalman, R. Thermoelectricity in Fullerene Metal Heterojunctions. *Nano Lett.* **2011**, *11*, 4089–4094.

(10) Evangeli, C.; Gillemot, K.; Leary, E.; González, M. T.; Rubio-Bollinger, G.; Lambert, C. J.; Agraït, N. Engineering the Thermopower of C_{60} Molecular Junctions. *Nano Lett.* **2013**, *13*, 2141−2145.

(11) Lee, S. K.; Ohto, T.; Yamada, R.; Tada, H. Thermopower of Benzenedithiol and C_{60} Molecular Junctions with Ni and Au Electrodes. *Nano Lett.* **2014**, *14*, 5276–5280.

(12) Rincón-García, L.; Ismael, A. K.; Evangeli, C.; Grace, I.; Rubio-Bollinger, G.; Porfyrakis, K.; Agraït, N.; Lambert, C. J. Molecular Design and Control of Fullerene-Based Bi-Thermoelectric Materials. *Nat. Mater.* **2016**, *15*, 289–293.

(13) Reddy, P.; Jang, S.-Y.; Segalman, R. A.; Majumdar, A. Thermoelectricity in Molecular Junctions. *Science*, **2007**, *315*, 1568–1571.

(14) Chang, W. B.; Mai, C.-K.; Kotiuga, M.; Neaton, J. B.; Bazan, G. C.; Segalman, R. A. Controlling the Thermoelectric Properties of Thiophene-Derived Single-Molecule Junctions. *Chem. Mater.* **2014**, *26*, 7229–7235

(15) Kim, T.; Darancet, P.; Widawsky, J. R.; Kotiuga, M.; Quek, S. Y.; Neaton, J. B.; Venkataraman, L. Determination of Energy Level Alignment and Coupling Strength in 4,4′-Bipyridine Single-Molecule Junctions. *Nano Lett.* **2014**, *14*, 794–798.

(16) Baheti, K.; Malen, J. A.; Doak, P.; Reddy, P.; Jang, S.-Y.; Tilley, T. D.; Majumdar, A.; Segalman, R. A. Probing the Chemistry of Molecular Heterojunctions Using Thermoelectricity. *Nano Lett*. **2008**, *8*, 715–719.

(17) Malen, J. A.; Doak, P.; Baheti, K.; Tilley, T. D.; Segalman, R. A.; Majumdar, A. Identifying the Length Dependence of Orbital Alignment and Contact Coupling in Molecular Heterojunctions. *Nano Lett*. **2009**, *9*, 1164–1169.

(18) Guo, S.; Zhou, G.; Tao, N. Single Molecule Conductance, Thermopower, and Transition Voltage. *Nano Lett*. **2013**, *13*, 4326–4332.

(19) Miao, R.; Xu, H.; Skripnik, M.; Cui, L.; Wang, K.; Pedersen, K. G. L.; Leijnse, M.; Pauly, F.; Wärnmark, K.; Meyhofer, E.; Reddy, P.; Linke, H. Influence of Quantum Interference on the Thermoelectric Properties of Molecular Junctions. *Nano Lett*. **2018**, *18*, 5666–5672.

(20) Hines, T.; Diez-Perez, I.; Hihath, J.; Liu, H.; Wang, Z-S.; Zhao, J.; Zhou, G.; Müllen, K.; Tao, N. Transition from Tunneling to Hopping in Single Molecular Junctions by Measuring Length and Temperature Dependence. *J. Am. Chem. Soc.* **2010**, *132*, 11658–11664.

(21) Haiss, W.; Wang, C.; Jitchati, R.; Grace, I.; Martin, S.; Batsanov, A. S.; Higgins, S. J.; Bryce, M. R.; Lambert, C. J.; Jensen, P. S. et. al. Variable Contact Gap Single-Molecule Conductance Determination for a Series of Conjugated Molecular Bridges. *J. Phys.: Condens. Matter* **2008**, *20*, 374119.

(22) Vonlanthen, D. Mishchenko, A.; Elbing, M.; Neuburger, M.; Wandlowski, T.; Mayor, M. Chemically Controlled Conductivity: Torsion-Angle Dependence in a Single-Molecule Biphenyldithiol Junction. *Angew. Chem. Int. Ed.* **2009**, *48*, 8886–8890.

(23) Klausen, R. S.; Widawsky, J. R.; Su, T. A.; Li, H.; Chen, Q.; Steigerwald, M. L.; Venkataraman, L.; Nuckolls, C. Evaluating Atomic Components in Fluorene Wires. *Chem. Sci.* **2014**, *5*, 1561–1564.

(24) Gantenbein, M.; Wang, L.; Al-Jobory, A. A.; Ismael, A. K.; Lambert, C. J.; Hong, W. J.; Bryce, M. R. Quantum Interference and Heteroaromaticity of *Para*- and *Meta*-Linked Bridged Biphenyl Units in Single Molecular Conductance Measurements. *Sci. Rep.* **2017**, *7*, 1794.

(25) Zhao, X.; Li, X.; Zhao, Y.; Zhang, J.; Pan, J.; Zhou, J. Amplified Spontaneous Emission from 2,7-Bis(4-pyridyl)fluorene-Doped DNA-Cetyltrimethyl Ammonium Complex Films. *Opt. Eng.* **2013**, *52*, 106109–106109.

(26) Niu, Z.; Li, D.; Liu, D.; Xia, D.; Zou, Y.; Sun, W.; Li, G. Syntheses, Electrochemical Behaviors, Spectral Properties and DFT Calculations of Two 1,3-Dithiole Derivatives. *Chem. Res. Chin. Univ.* **2014**, *30*, 425–430.

(27) Amara, J. P.; Swager, T. M. Conjugated Polymers with Geminal Trifluoromethyl Substituents Derived from Hexafluoroacetone. *Macromolecules* **2006**, *39*, 5753–5759.

(28) Babadzhanova, L. A.; Kirij, N. V.; Yagupolskii, Y. L.; Tyrra, W.; Naumann, D. Convenient Syntheses of 1,1,1,3,3,3-Hexafluoro-2-organyl-propan-2-ols and the Corresponding Trimethylsilyl Ethers. *Tetrahedron* **2005**, *61*, 1813–1819.

(29) Soler, J. M.; Artacho, E.; Gale, J. D.; Garcia, A.; Junquera, J.; Ordejon, P.; Sanchez-Portal, D. The SIESTA Method for *ab initio* Order-*N* Materials Simulation. *J. Phys.: Condens. Matter* **2002**, *14*, 2745–2779.

(30) Ferrer, J.; Lambert, C. J.; Garcia-Suarez, V. M.; Manrique, D. Z.; Visontai, D.; Oroszlany, L.; Rodriguez-Ferradas, R.; Grace, I.; Bailey, S. W. D.; Gillemot, K. *et al.* GOLLUM: a Next-

Generation Simulation Tool for Electron, Thermal and Spin Transport. *New J. Phys.* **2014**, *16*, 093029.

(31) Lof, R. W.; van Veenendaal, M. A.; Koopmans, B.; Jonkman, H. T.; Sawatzky, G. A. Band Gap, Excitons, and Coulomb Interaction in Solid C60. *Phys. Rev. Lett.* **1992**, *68*, 3924–3927.

(32) Hung, Y-C.; Jiang, J-C.; Chao, C-Y.; Su, W-F.; Lin, S-T. Theoretical Study on the Correlation Between Band Gap, Bandwidth, and Oscillator Strength in Fluorene-Based Donor-Acceptor Conjugated Copolymers. *J. Phys. Chem. B* **2009**, *113*, 8268–8277.

(33) Claughton, N. R.; Leadbeater, M.; Lambert, C. J. Theory of Andreev Resonances in Quantum Dots. *J. Phys.: Condens. Matter* **1995**, *7*, 8757.

TOC Graphic

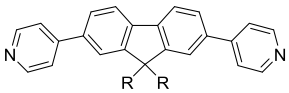

1 R = H **FI-H**
2 R = Me **FI-Me**
3 R = OMe **FI-OMe**
4 R = CF_3 **FI-CF_3**

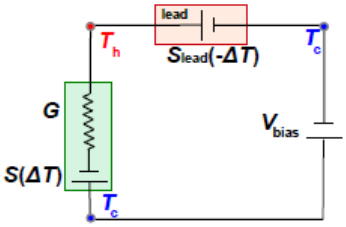

Supporting Information

Thermoelectric Properties of 2,7-Dipyridylfluorene Derivatives in Single-Molecule Junctions

Gilles Yzambart,[†,∃] Laura Rincón-García,[‡,§,∃] Alaa A. Al-Jobory,[‖,⊥,∃] Ali K. Ismael, [‖,#,∃] Gabino Rubio-Bollinger,[‡,○] Colin J. Lambert,*[,‖] Nicolás Agraït,*[‡,§,○] Martin R. Bryce*[,†]

[†] Department of Chemistry, Durham University, Durham DH1 3LE, UK

[‡] Departamento de Física de la Materia Condensada, Universidad Autónoma de Madrid, E-28049 Madrid, Spain

[§] Instituto Madrileño de Estudios Avanzados en Nanociencia IMDEA-Nanociencia, E-28049 Madrid, Spain

[‖] Department of Physics, Lancaster University, LA1 4YB, UK

[⊥] Department of Physics, College of Education for Pure Science, Anbar University, Anbar, Iraq

[#] Department of Physics, College of Education for Pure Science, Tikrit University, Tikrit, Iraq

[○] Condensed Matter Physics Center (IFIMAC) and Instituto Universitario de Ciencia de Materiales "Nicolás Cabrera", Universidad Autónoma de Madrid, E-28049 Madrid, Spain

[∃] These authors contributed equally to this work.

Table of Contents

1. Theoretical calculations

a. Geometry of isolated molecules and their junctions

The DFT code (SIESTA) was used to obtain fully relaxed geometries of the isolated fluorene molecules, as shown in Figure S1.

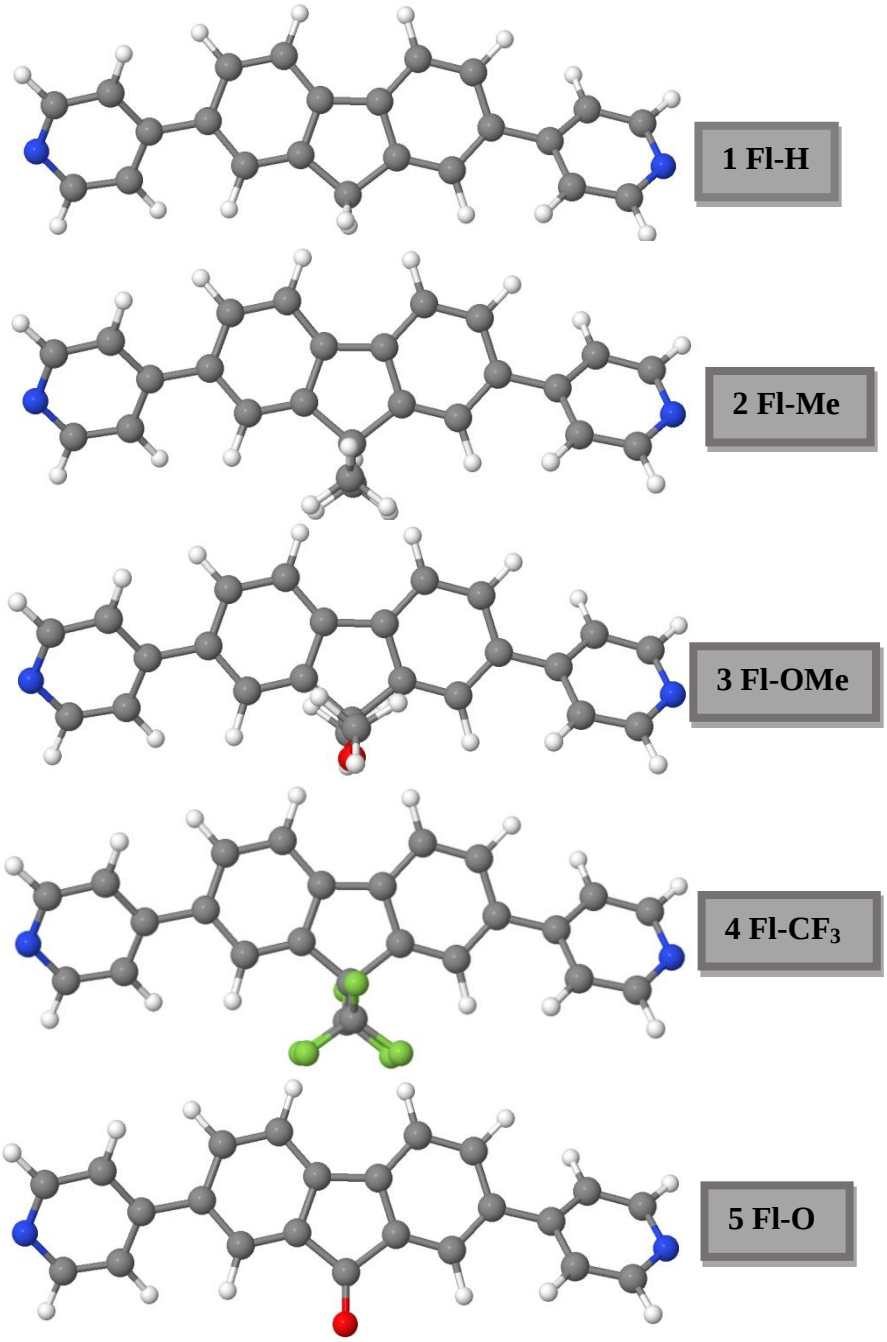

Figure S1. Fully relaxed isolated fluorene molecules: **1** Fl-H, **2** Fl-Me, **3** Fl-OMe, **4** Fl-CF_3 and **5** Fl-O (top to bottom).

The series of molecules were then connected to gold electrodes and the geometries were relaxed. The structures are shown in Figure S2.

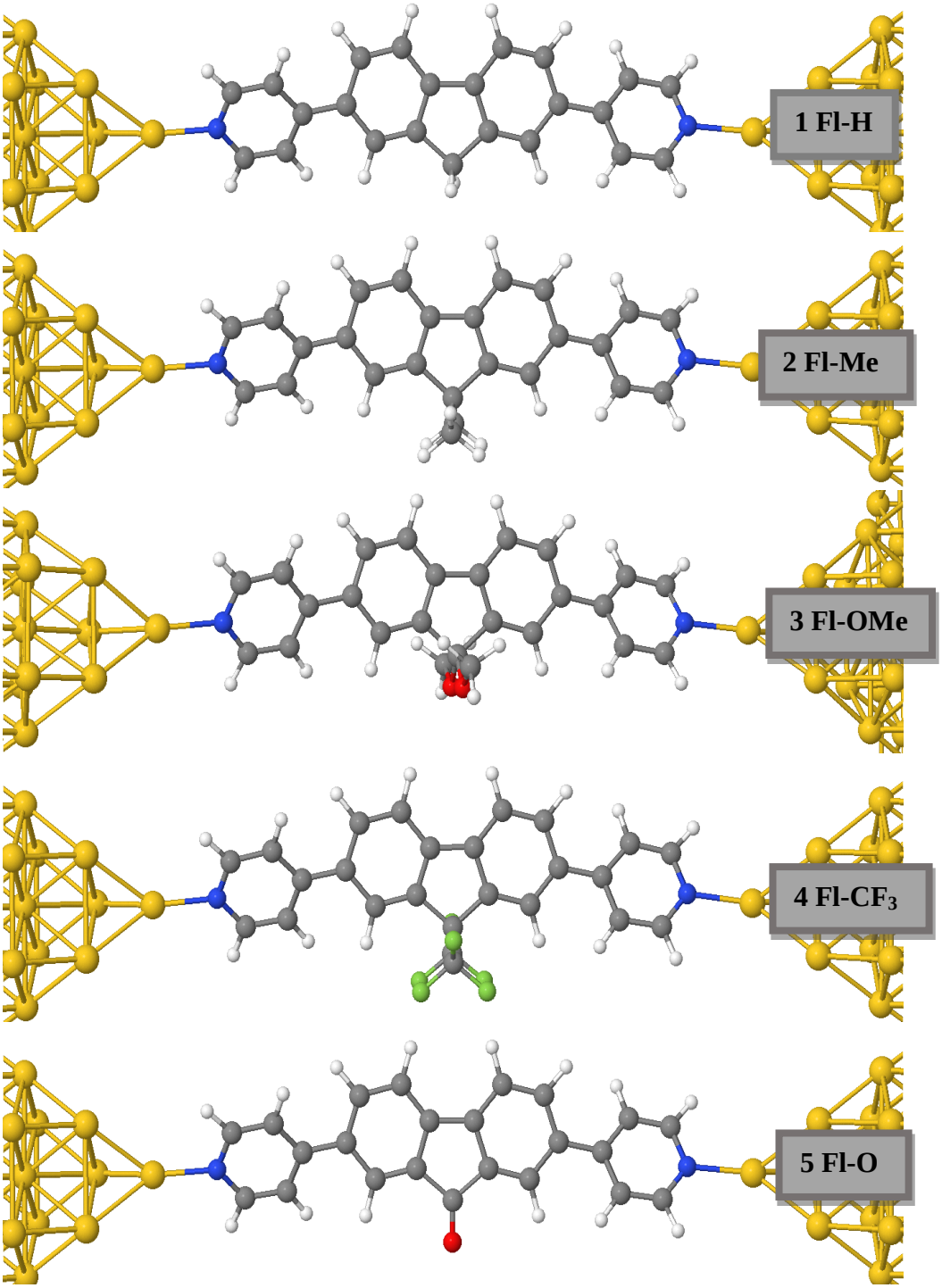

Figure S2. Fluorene derivatives in Au|molecule|Au junctions: **1** Fl-H, **2** Fl-Me, **3** Fl-OMe, **4** Fl-CF_3 and **5** Fl-O (top to bottom).

b. Binding energy of 4 Fl-CF_3 on gold

To calculate the optimum binding distance for the fluorene series between two gold(111) surfaces, DFT and the counterpoise method were used, which removes basis set superposition errors (BSSE). The binding distance z was defined as the distance between the gold surface and the N atom of the molecule. The ground state energy of the total system was calculated using SIESTA and is denoted E_{AB}^{AB}, with the parameters defined in the experimental section of the main text. Here the gold leads consist of 6 layers of 30 atoms. The energy of each monomer was then calculated in a fixed basis, which is achieved through the use of ghost atoms in SIESTA. Hence the energy of the individual molecule in the presence of the fixed basis is defined as E_A^{AB} and for the isolated gold as E_B^{AB}. The binding energy is then calculated using the following equation S1:

$$\text{Binding Energy} = E_{AB}^{AB} - E_A^{AB} - E_B^{AB} \qquad \text{(S1)}$$

As an example, Figure S3 shows the binding energy calculation for molecule **4**. Almost identical binding energies were obtained for the other four molecules **1-3** and **5**.

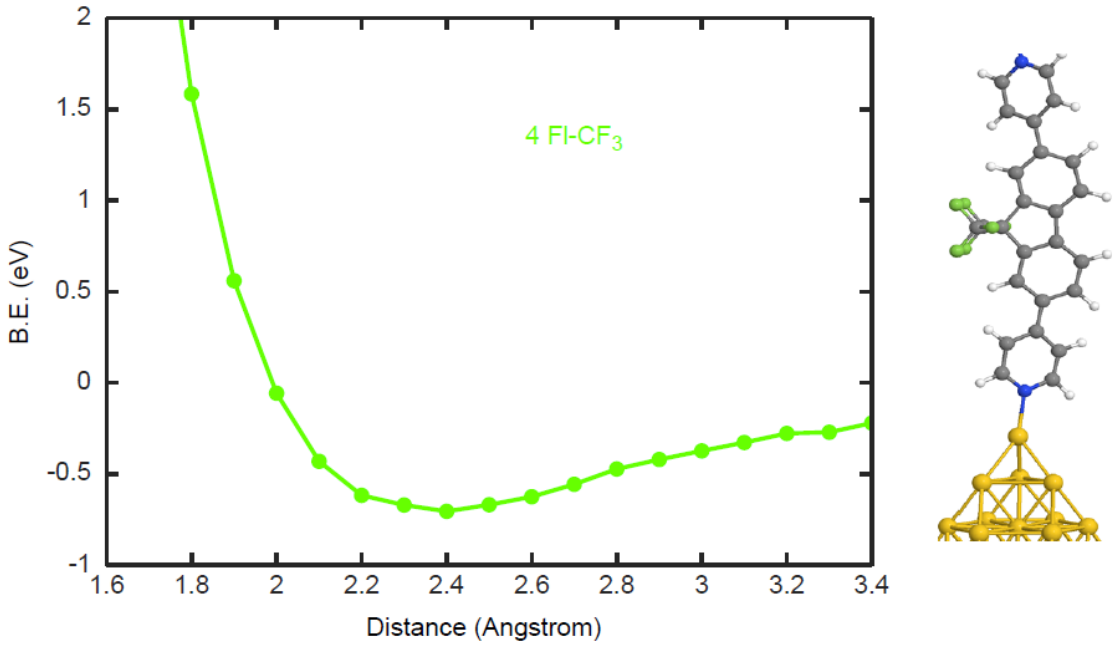

Figure S3. Left panel: Binding energy of **4** attached to gold as a function of molecule-contact distance. The equilibrium distance (i.e. the minimum of the binding energy curve) is approximately 2.4 Å for **4**. Right panel: molecule **4** attached to a gold lead.

c. Wave function plots.

The plots below show the isosurfaces of the HOMO, LUMO, HOMO-1 and LUMO+1 of the isolated molecules **1-5**.

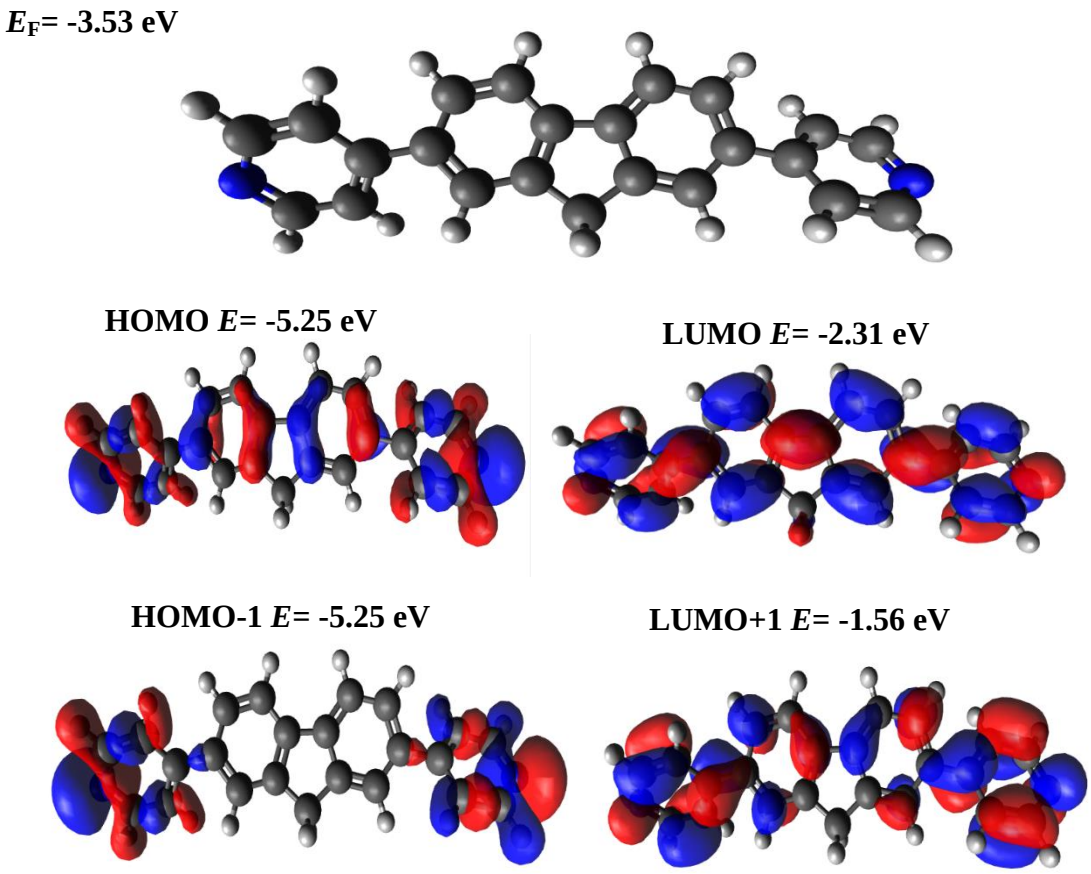

Figure S4. Wave function for molecule **1** (Fl-H). Top panel: Fully optimized geometry. Lower panel: HOMO, LUMO, HOMO-1 and LUMO+1 with their energies.

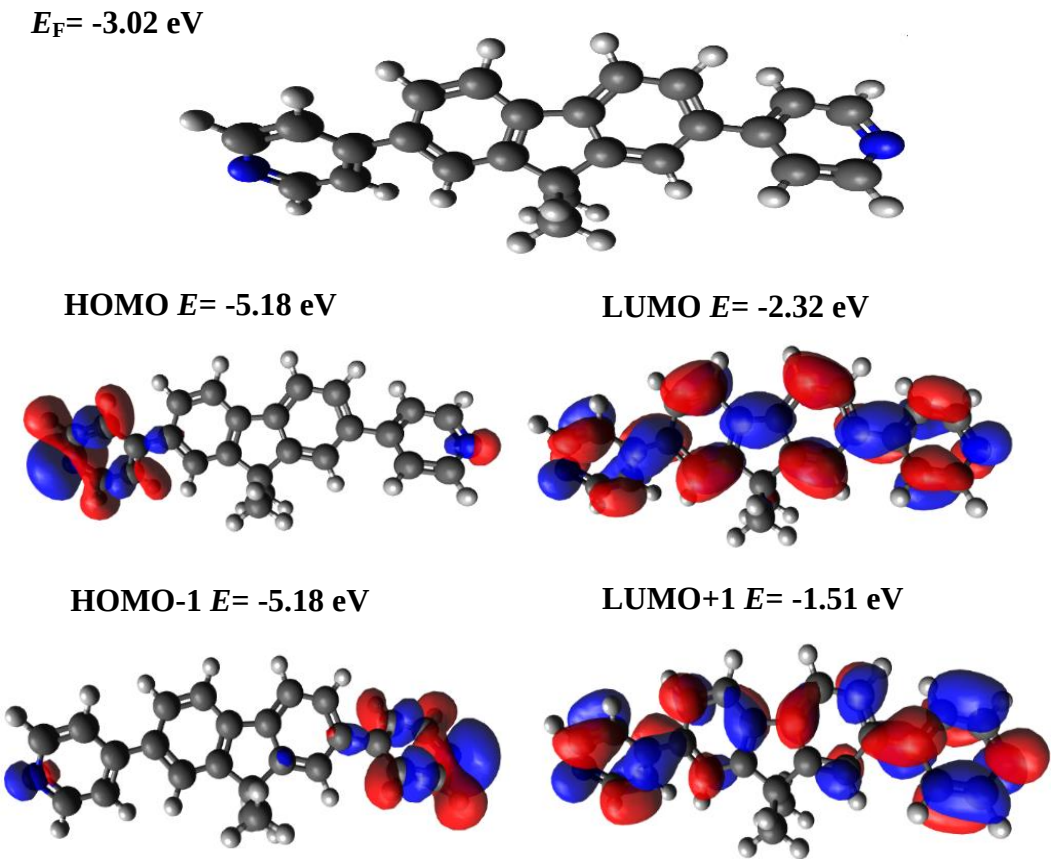

Figure S5. Wave function for molecule **2** (Fl-Me). Top panel: Fully optimized geometry. Lower panel: HOMO, LUMO, HOMO-1 and LUMO+1 with their energies.

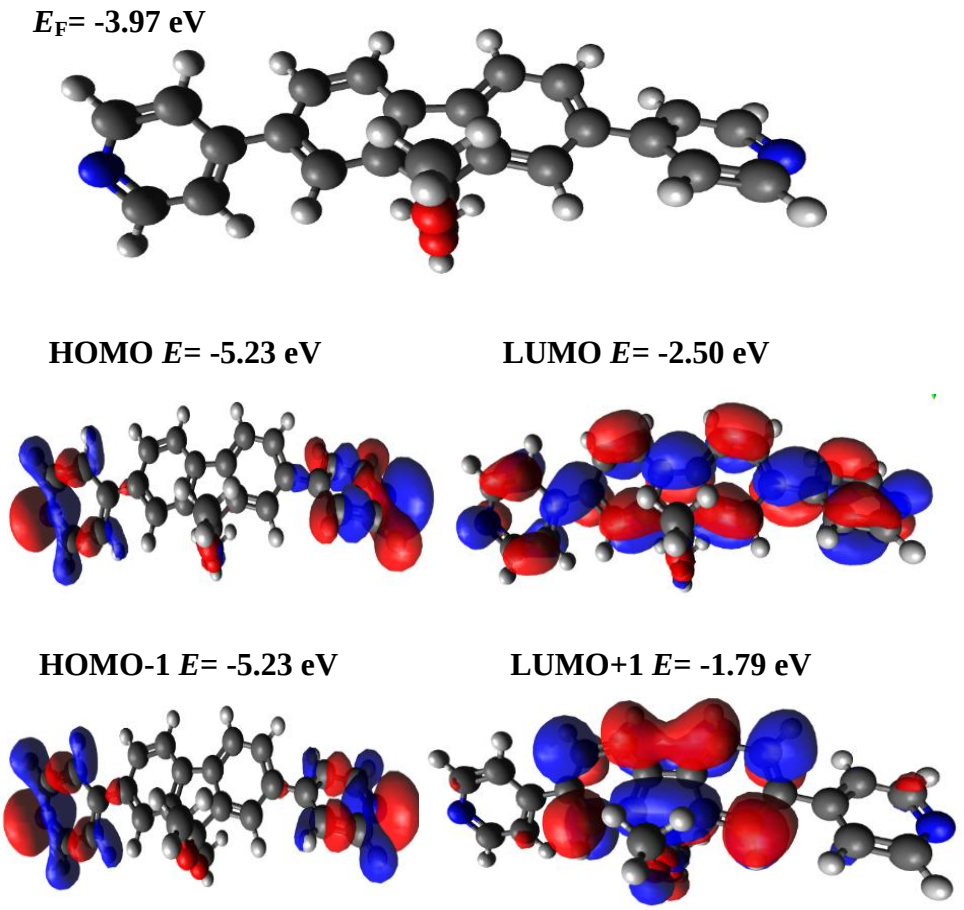

Figure S6. Wave function for molecule **3** (Fl-OMe). Top panel: Fully optimized geometry. Lower panel: HOMO, LUMO, HOMO-1 and LUMO+1 with their energies.

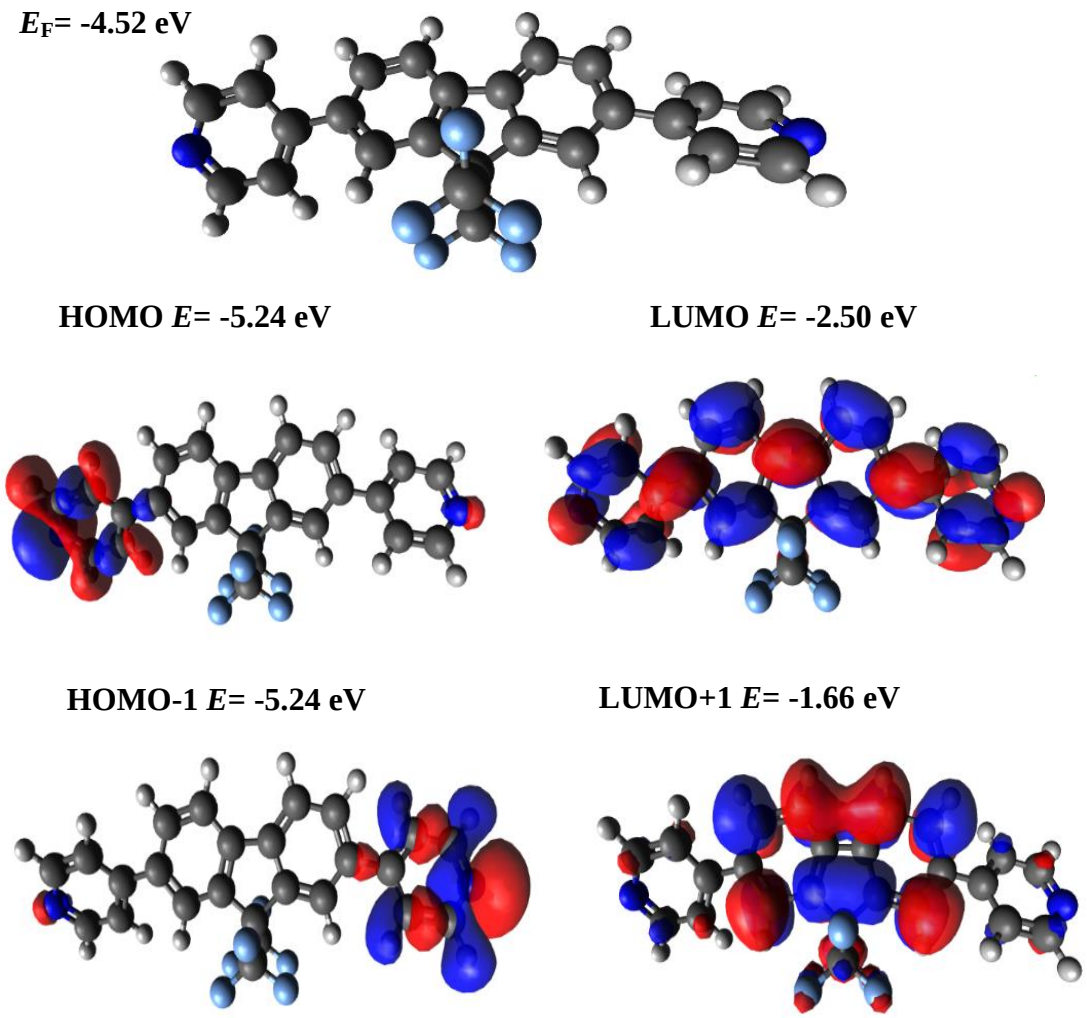

Figure S7. Wave function for molecule **4** (Fl-CF_3). Top panel: Fully optimized geometry. Lower panel: HOMO, LUMO, HOMO-1 and LUMO+1 with their energies.

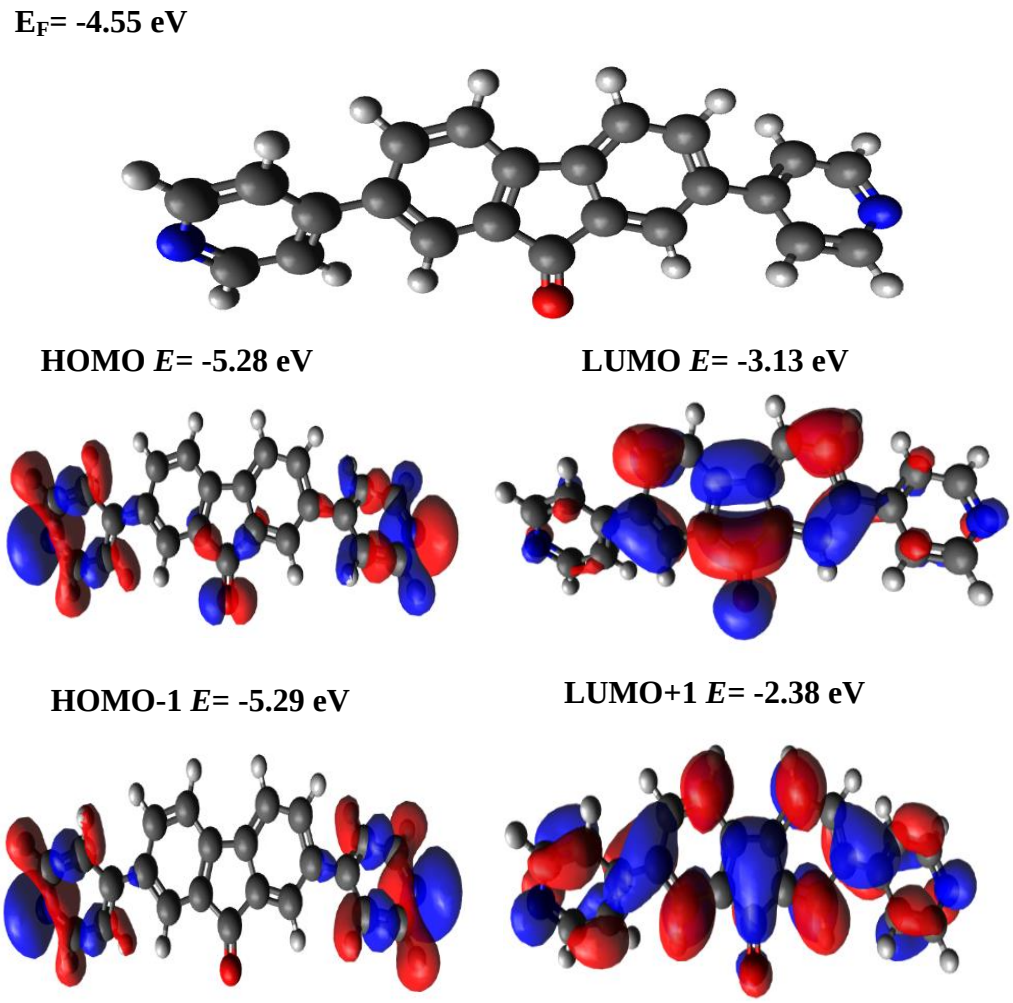

Figure S8. Wave function for molecule **5** (Fl-O). Top panel: Fully optimized geometry. Lower panel: HOMO, LUMO, HOMO-1 and LUMO+1 with their energies.

Figures S4-S7 show that there is no frontier orbital distribution on the pendant group for molecules **1-4**, whereas Figure S8 shows a contribution of the HOMO, LUMO and LUMO+1 on the oxygen atom of fluorenone derivative **5**. This distribution clearly appears in the transmission curve of **5** as a resonance in Figure S9. This feature will be discussed in more detail later in the theoretical model (Section 1f). The HOMOs of these molecules are degenerate as shown in the left panels of Figures S4-S8.

d. HOMO-LUMO gaps

The calculated and optically measured HOMO-LUMO gaps are listed in Table S1. Theoretical gaps were calculated for isolated molecules and when the molecules are in the junctions, the gap between their HOMO and LUMO transmission resonances is quoted. As shown by the third and fourth columns in Table S1, isolated gaps are larger than the gaps between the transmission resonances. This is because the latter are shifted by the real part of the self-energy of the contact to the leads, reflecting the fact that the system is more open when contacted to electrodes. To obtain a more accurate HOMO-LUMO gap, we use a scissor correction as described in the main text.

Table S1: Experimental measurements and theoretical calculations of HOMO–LUMO gaps in eV.

Molecule	[a] E_{g} (Exp.)	[b] $E_{g,\,DFT}$ (Iso.)	[c] $E_{g,\,DFT}$ (Au|M|Au)
1 Fl-H	3.80	2.85	2.56
2 Fl-Me	3.78	2.83	2.54
3 Fl-OMe	3.84	2.69	2.54
4 Fl-CF_3	3.95	2.69	2.61
5 Fl-O	3.84	2.51	2.42

[a] Experimental data: $E_g = 1240/\lambda_{onset\ Abs.}$ [b] Theoretical HOMO–LUMO gaps for the isolated molecules.
[c] Theoretical gaps between HOMO–LUMO transmission resonances in Au|molecule|Au structures.

e. Transmission coefficients

The transmission coefficient $T(E)$ was calculated for the fluorene molecules **1-5**. Figure S9 suggests that the conductance values of **1-4** are approximately the same when the Fermi energy lies in the tail of the LUMO. The $T(E)$ of **5** has a resonance close to E= -2.0 eV. This is consistent with the HOMO wave function plot in Figure S8, which shows a significant weight on the oxygen atom.

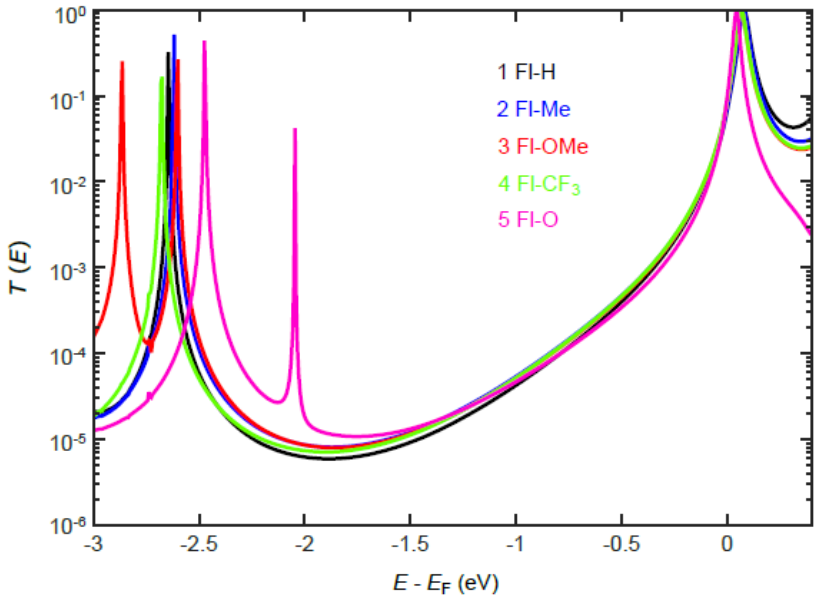

Figure S9. Transmission coefficients $T(E)$ for molecules **1-5** (without scissor correction).

f. Theoretical model for 5 Fl-O

Although the resonance at E= -2 eV is far from the expected experimental Fermi energy and therefore does not affect the electrical conductance, it is of interest theoretically to explore its origin. The HOMO plot for molecule **5** in Figure S8 shows a significant weight on the oxygen atom. To prove that this bound state is the origin of the transmission resonance near E= -2 eV, the following plots show the effect on the transmission coefficient of moving a water molecule dipole gradually away from the pendant oxygen atom (see top panel of Fig S10).

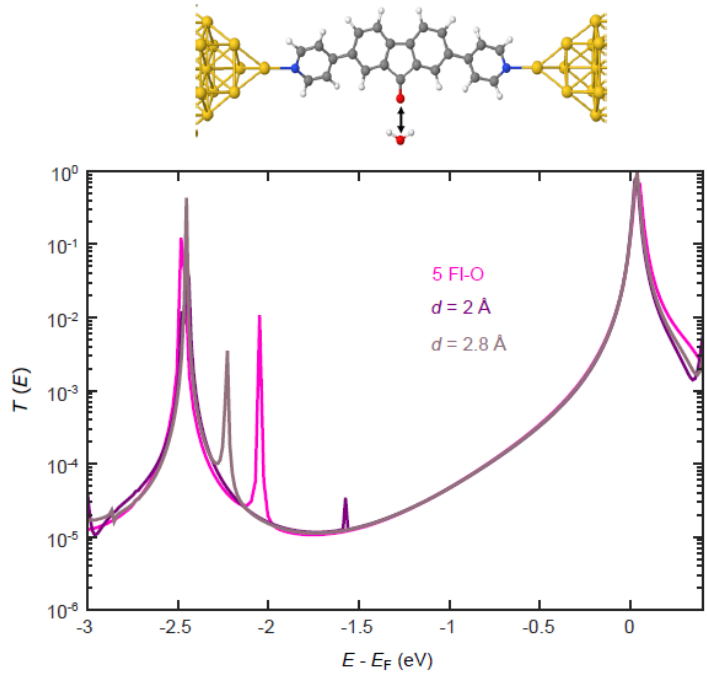

Figure S10. Zero bias transmission coefficient $T(E)$ of a gating model (**5** Fl-O), curves labelled *d* when a water molecule is present at two distances 2.0 and 2.8 Å.

Figure S10 lower panel shows the effect of this electrostatic gating process. During successive gating steps the transmission resonances move from higher energy to lower energy when **5** is in the vicinity of a water molecule. The molecules **2-4** with pendant Me, OMe and CF_3 groups also have resonances due to the pendant groups.[1] However, these resonances are outside the HOMO-LUMO gap and therefore are not relevant experimentally.

g. Seebeck coefficient

Figure S11 shows that the five molecules possess a similar Seebeck coefficient, in agreement with the experimental measurements.

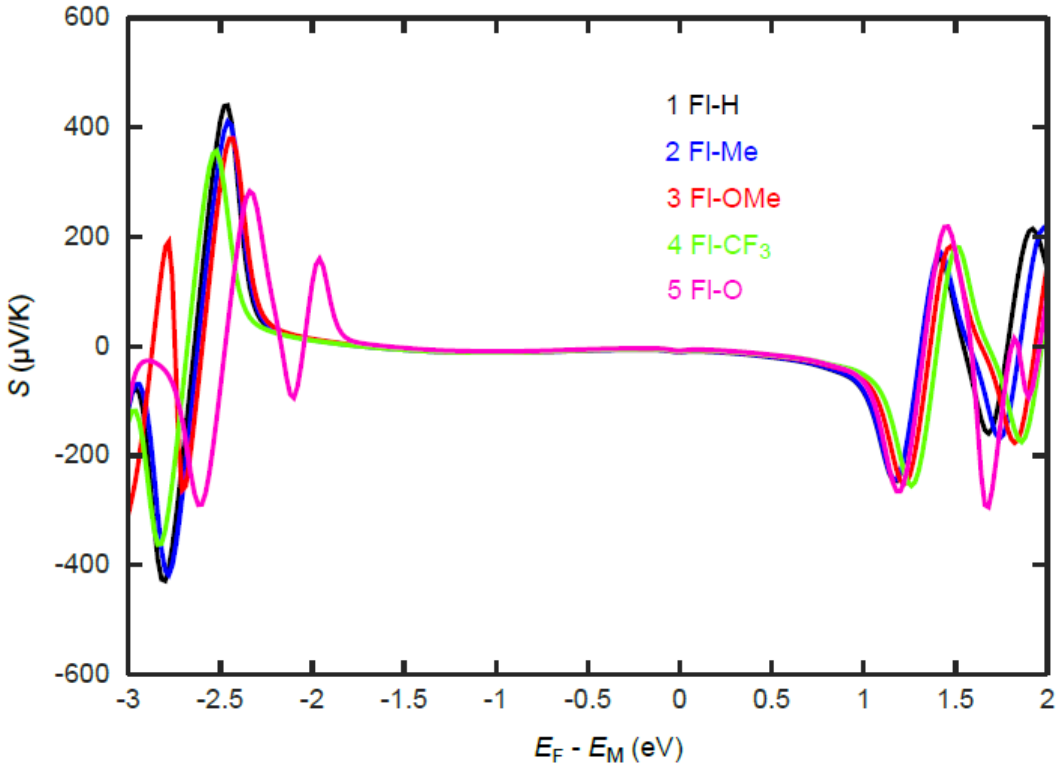

Figure S11. Calculated Seebeck coefficient *S* of **1-5** using scissor corrections.

2. Molecular synthesis

a. General details

376 or 400 MHz NMR spectra were recorded on Bruker Avance-400 MHz instruments. Chemical shifts are reported in ppm and referenced to TMS or residual solvent. ^{13}C NMR

(151 or 176 MHz) spectral data were collected on Varian VNMRS-700 MHz spectrometers. All melting points were measured using a Stuart SMP40 melting point apparatus. The temperatures at the melting point were ramped at 1 ^{o}C/min and are uncorrected. Elemental analysis was performed at the Elemental Microanalysis Service of Durham University (UK) using an Exeter CE-400 Elemental Analyzer. MALDI TOF MS Mass spectrometry and high resolution mass spectra were obtained using a Autoflex II ToF/ToF (Bruker) and a LCT Premier XE (Waters) respectively. All chemicals were purchased from Acros Organics, Sigma Aldrich or Alfa Aesar and used without further treatment. Dry solvents were obtained from a solvent purification system. All air-sensitive reactions were conducted under a blanket of argon which was dried by passage through a column of phosphorus pentoxide. Column chromatography was performed using silica gel from Sigma Aldrich. UV-Visible absorption spectra were recorded at room-temperature using a UV-Visible spectrophotometer Evolution 220 from Thermo Scientific. Photoluminescence spectra were recorded on a Horiba Jobin Yvon SPEX Fluorolog 3-22 spectrofluorometer in quartz cuvettes with a path length of 10 mm.

b. Synthetic procedures

***α,α*-bis(trifluoromethyl)-1,1'-biphenyl-2-methanol B**

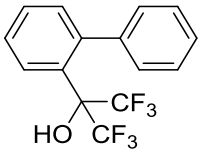

A solution of 2-biphenylcarbonyl chloride **A**[2] (4.23 g, 19.5 mmol) in dry 1,2-dimethoxyethane (50 mL) was cooled to -60 ^{o}C. Then, Me_3SiCF_3 (5.77 mL, 39.0 mmol) and $[Me_4N]F$ (3.63 g, 39.0 mmol) were added and the solution was stirred at -30 ^{o}C for 1 h. The reaction was then allowed to warm at room temperature and was stirred for 18 h under argon. An aqueous solution of HCl (50 mL, 2 M) was added, the organic layer was extracted with ether, washed with water (20 mL), dried over $MgSO_4$ and the solvent was evaporated. The addition of hexane to the mixture led to the formation of a white precipitate which was filtered off. The filtrate was purified by column chromatography on silica gel using hexane with a gradient of EtOAc (0 – 15%) as eluent. The product **B** was isolated as colorless crystals (1.78 g, 30%). ^{1}H NMR (400 MHz, $CDCl_3$): δ 7.77 (1H, m), 7.46 (5H, m), 7.37 (1H,

m), 3.45 (1H, s). ^{19}F NMR (376 MHz, $CDCl_3$): δ -74.98 (6F, s). These data are in agreement with the literature data for **B** synthesized by a different route.[3]

2,7-diiodo-9,9-di(trifluoromethyl)fluorene D

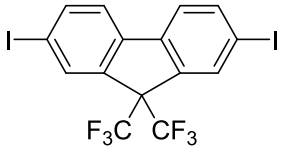

B was converted into **C** (82% yield) and **C** was converted into **D** as described in the literature.[3] **D** (470 mg, 62%) was characterized as follows: ^{1}H NMR (400 MHz, $CDCl_3$): δ 8.07 (2H, s), 7.91 (2H, dd, *J* = 8.1, 1.5 Hz), 7.50 (2H, d, *J* = 8.1 Hz), 3.45 (1H, s). ^{19}F NMR (376 MHz, $CDCl_3$): δ -68.23 (6F, s). These data are in agreement with the literature.[3]

2,7-dibromo-9,9-dimethoxyfluorene

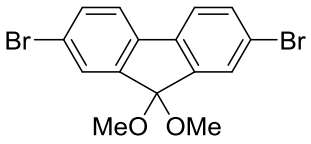

Concentrated H_2SO_4 (0.24 mL, 4.44 mmol) and dry trimethylorthoformilate (4.88 mL, 46.80 mmol) were added to a suspension of 2,7-dibromo-9-fluorenone (1.0 g, 2.96 mmol) in dry methanol (200 mL). The reaction was stirred for 48 h at reflux and then cooled to room temperature prior to the addition of Et_3N (until pH 7 was achieved). The white precipitate was filtered off and washed with MeOH. Then the filtrate was concentrated under high vacuum; the precipitate was again filtered and washed as above. Recrystallization in hexane gave white crystals of 2,7-dibromo-9,9-dimethoxyfluorene (1.14 g, 98%). mp: 180.0 ^{o}C. ^{1}H NMR (400 MHz, $CDCl_3$): δ 7.66 (2H, dd, *J* = 1.8, 0.6 Hz), 7.54 (2H, dd, *J* = 8.1, 1.8 Hz), 7.44 (2H, dd, *J* = 8.01, 0.6 Hz), 3.36 (6H, s). ^{13}C NMR (101 MHz, $CDCl_3$): δ 143.76, 138.19, 133.56, 128.34, 122.51, 121.91, 107.36, 52.10. Anal Calcd for $C_{15}H_{12}Br_2O_2$: C 46.91, H 3.15; found C 47.19, H 3.23.

2,7-dipyridinyl-9,9-dimethylfluorene 2

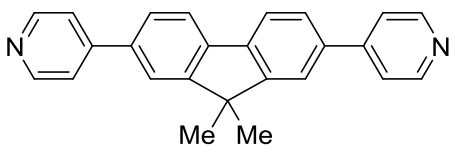

2,7-dibromo-9,9-dimethylfluorene (500 mg, 1.43 mmol), 4-pyridyl boronic acid (440 mg, 3.57 mmol), Na_2CO_3 (606 mg, 5.72 mmol) and $Pd(PPh_3)_4$ (545 mg, 0.47 mmol) were disolved in a degassed mixture of 1,2-dimethoxyethane/distilled water (40 mL/20 mL). After 24 h of stirring at reflux under argon, the reaction was cooled to room temperature, extracted with DCM and dried over $MgSO_4$. Purification performed through silica gel using DCM with a gradient of EtOAc (from 0 to 90%) followed by recrystallization in MeOH gave white crystals of **2** (330 mg, 66%). mp: 224.1 ^{o}C. ^{1}H NMR (400 MHz, $CDCl_3$): δ 8.68 (4H, dd, *J* = 4.4, 1.7 Hz), 7.83 (2H, dd, *J* = 7.9, 0.6 Hz), 7.71 (2H, d, *J* = 1.2 Hz), 7.63 (2H, dd, *J* = 7.9, 1.7 Hz), 7.57 (4H, dd, *J* = 4.4, 1.7 Hz), 1.59 (6H, s). ^{13}C NMR (101 MHz, $CDCl_3$): δ 155.17, 150.56, 148.69, 139.66, 137.94, 126.61, 121.88, 121.56, 121.24, 47.51, 27.45. HRMS-ASAP^{+}, calcd for $C_{25}H_{20}N_2$: 348.1626; found (m/z): 348.1615. Anal Calcd for $C_{25}H_{20}N_2$: C 86.17, H 5.79, N 8.04; found C 85.77, H 5.84, N 7.94.

2,7-dipyridinyl-9,9-dimethoxyfluorene 3

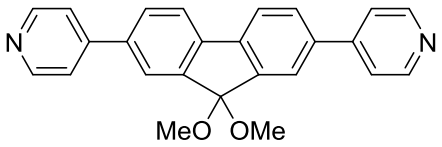

2,7-dibromo-9,9-dimethoxyfluorene (110 mg, 0.29 mmol), 4-pyridyl boronic acid (89 mg, 0.72 mmol), Na_2CO_3 (122 mg, 1.15 mmol) and $Pd(PPh_3)_4$ (115 mg, 0.10 mmol) were dissolved in a degassed mixture of 1,2-dimethoxyethane/distilled water (10 mL/5 mL). After 24 h of stirring at reflux under argon, the reaction was cooled to room temperature, extracted with DCM, dried over $MgSO_4$ and solvents were evaporated under high vacuum. Purification was performed on silica using as eluent a gradient of EtOAc in DCM (from 0 to 80%) followed by DCM with 3% of MeOH. Then recrystallization in acetonitrile gave a yellow

powder of **3** (60 mg, 55%). mp: 213.1 ^{o}C. ^{1}H NMR (400 MHz, $CDCl_3$): δ 8.70 (4H, dd, *J* = 4.5, 1.7 Hz), 7.85 (2H, d, *J* = 1.0 Hz), 7.78 (2H, dd, *J* = 7.9, 0.7 Hz), 7.74 (2H, dd, *J* = 7.9, 1.7 Hz), 7.58 (4H, dd, *J* = 4.5, 1.7 Hz), 3.44 (6H, s). ^{13}C NMR (101 MHz, $CDCl_3$): δ 150.77, 148.08, 143.45, 140.43, 138.68, 129.53, 123.57, 121.84, 121.52, 107.83, 52.23.

2,7-dipyridinyl-9,9-bis(trifluoromethyl)fluorene 4

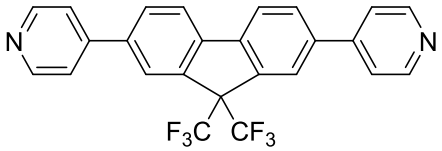

2,7-diiodo-9,9-bis(trifluoromethyl)fluorene **D** (200 mg, 0.36 mmol), 4-pyridyl boronic acid (111 mg, 0.90 mmol), Na_2CO_3 (153 mg, 1.44 mmol) and $Pd(PPh_3)_4$ (138 mg, 0.12 mmol) were dissolved in a degassed mixture of 1,2-dimethoxyethane/distilled water (12 mL/6 mL). After 24 h of stirring at reflux under argon, the reaction was cooled to room temperature, extracted with DCM and dried over $MgSO_4$. Purification on silica gel using hexane then a gradient of MeOH in EtOAc (from 0 to 5%) followed by a recrystallization in hexane led to the isolation of white crystals of **4** (110 mg, 67%). mp: 187.4 ^{o}C. ^{1}H NMR (400 MHz, $CDCl_3$): δ 8.73 (4H, dd, *J* = 4.4, 1.7 Hz), 8.04 (2H, s), 8.94 (2H, d, *J* = 7.9 Hz), 7.87 (2H, dd, *J* = 7.9, 1.7 Hz), 7.57 (4H, dd, *J* = 4.4, 1.7 Hz). ^{19}F NMR (376 MHz, $CDCl_3$): δ -68.15 (6F, s). ^{13}C NMR (101 MHz, $CDCl_3$): δ 150.80, 147.53, 142.70, 139.38, 136.31, 130.42, 125.37, 121.99, 121.96. HRMS-ES^{+}, calcd for $C_{25}H_{14}F_6N_2$: 456.1061; found (m/z) $[M+H]^{+}$: 457.1146.

d) Copies of NMR spectra

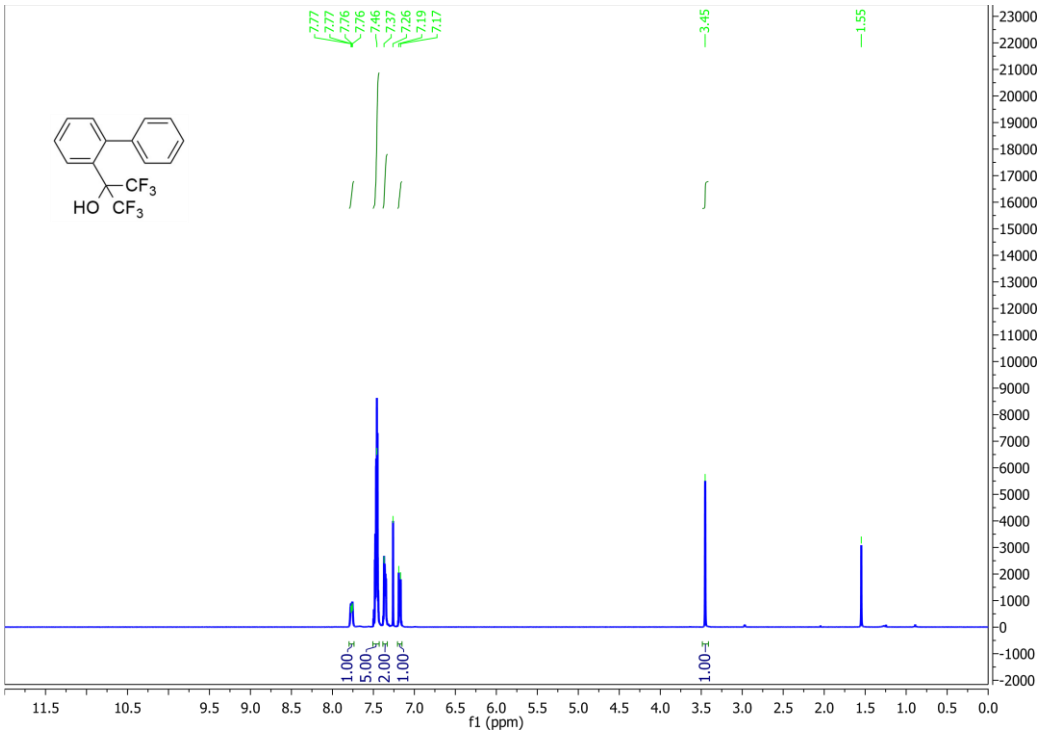

Figure S12. ^{1}H NMR spectrum of α,α-bis(trifluoromethyl)-1,1'-biphenyl-2-methanol **B**

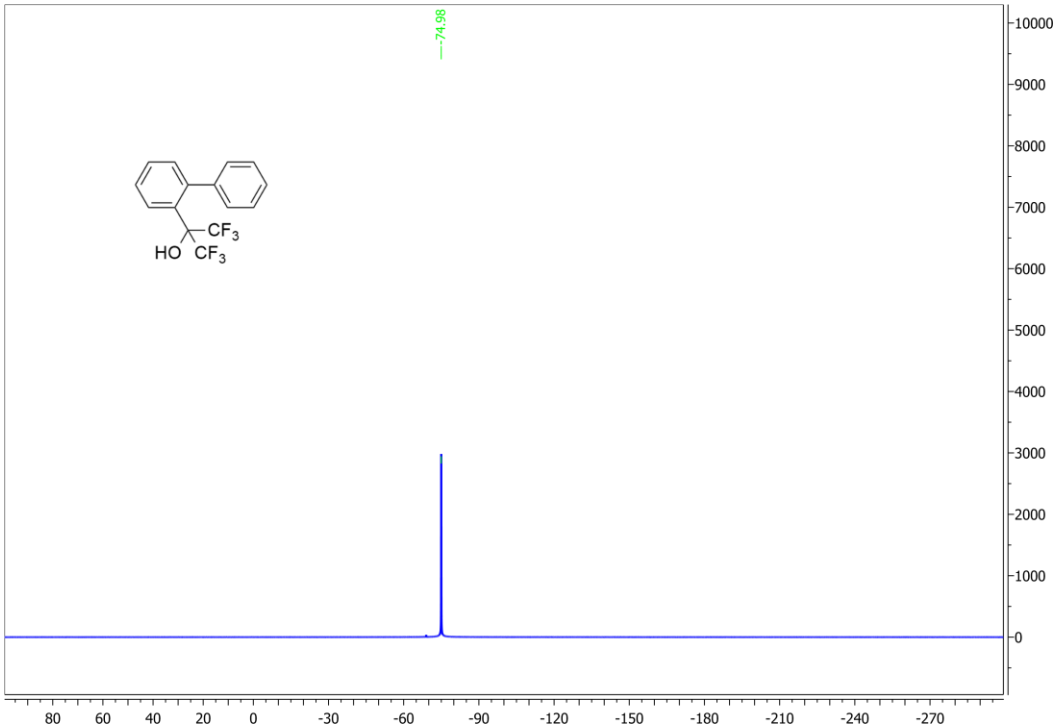

Figure S13. ^{19}F NMR spectrum of α,α-bis(trifluoromethyl)-1,1'-biphenyl-2-methanol **B**

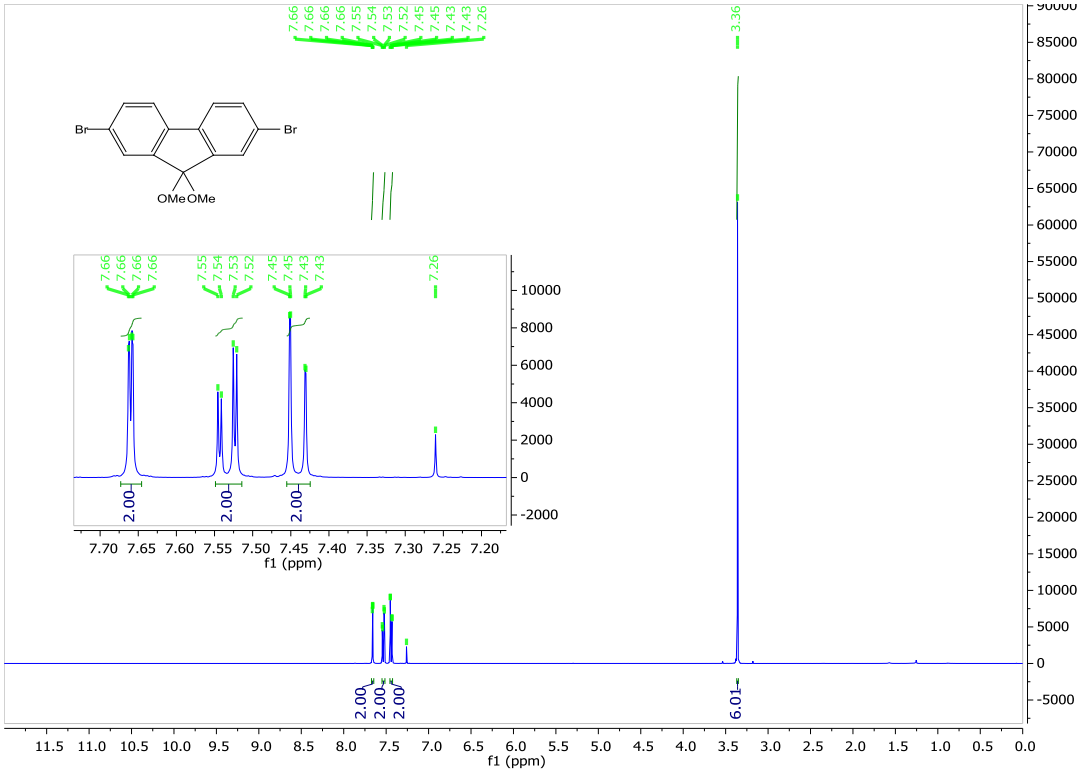

Figure S14. ^{1}H NMR spectrum of 2,7-dibromo-9,9-dimethoxyfluorene

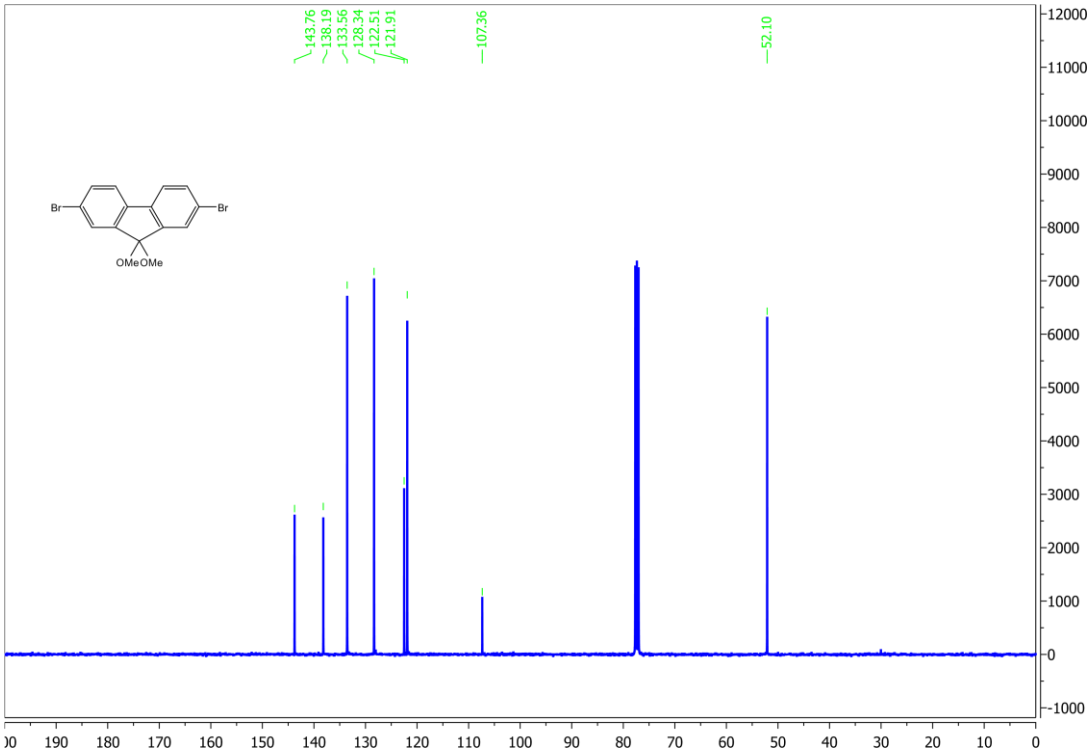

Figure S15. ^{13}C NMR spectrum of 2,7-dibromo-9,9-dimethoxyfluorene

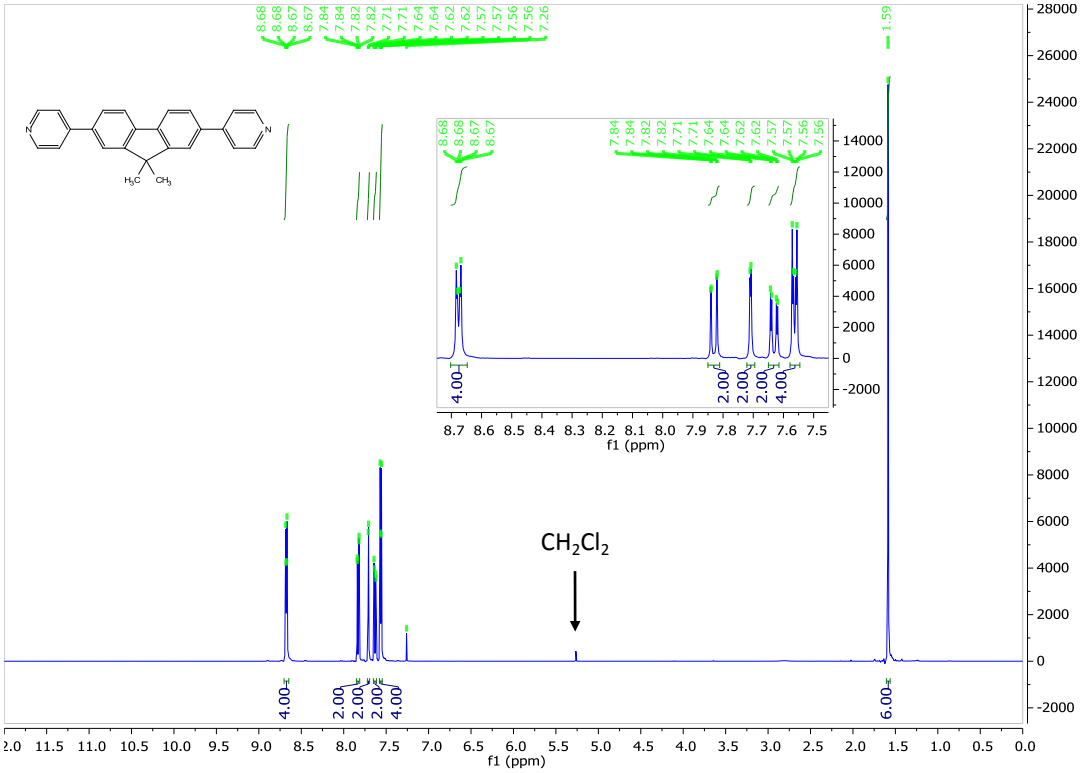

Figure S16. ^{1}H NMR spectrum of 2,7-dipyridinyl-9,9-dimethylfluorene **2**

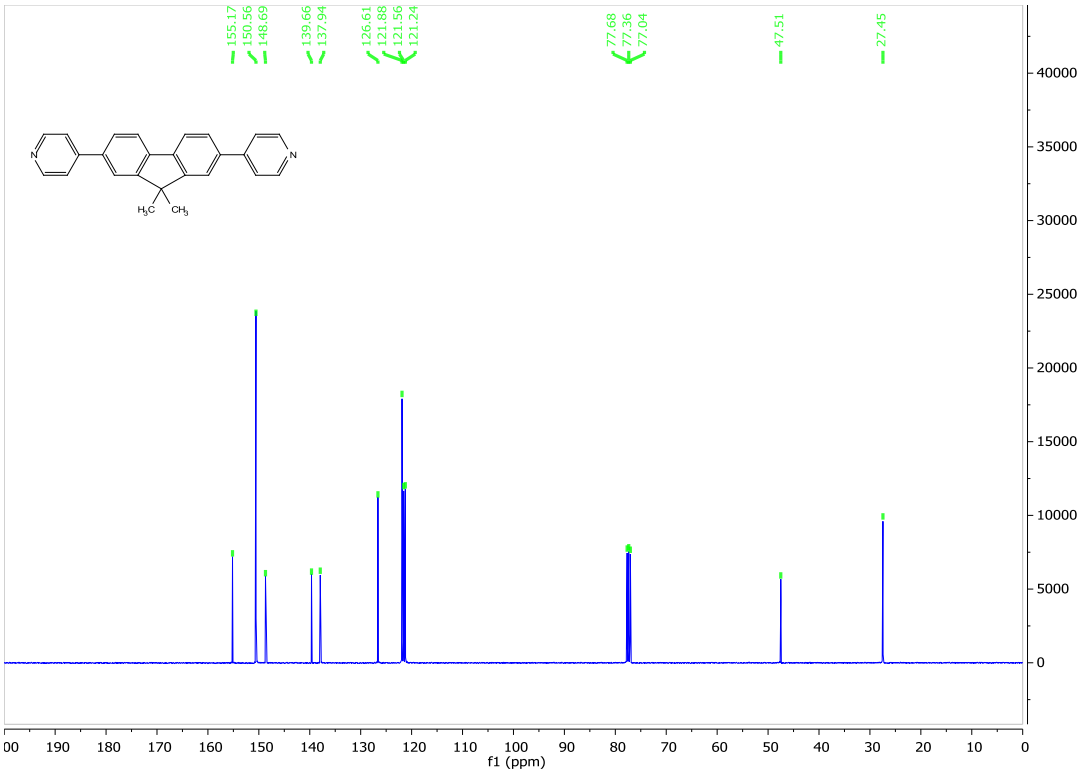

Figure S17. ^{13}C NMR spectrum of 2,7-dipyridinyl-9,9-dimethylfluorene **2**

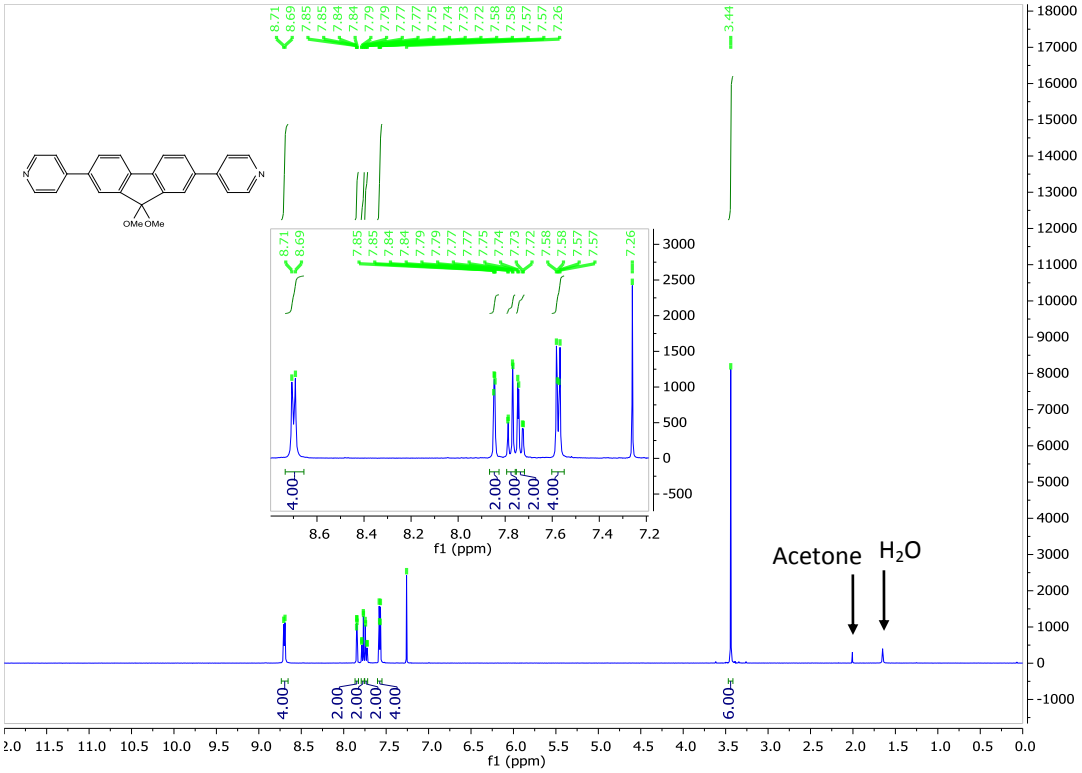

Figure S17. ^{1}H NMR spectrum of 2,7-dipyridinyl-9,9-dimethyoxyfluorene **3**

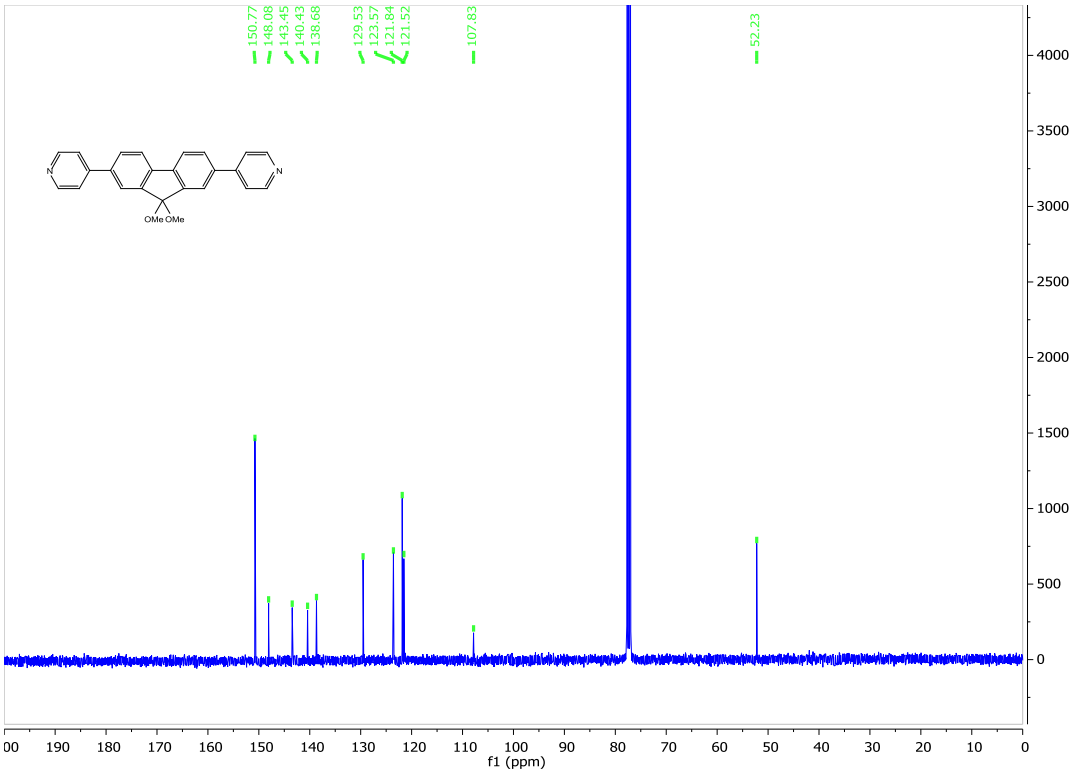

Figure S18. ^{13}C NMR spectrum of 2,7-dipyridinyl-9,9-dimethyoxyfluorene **3**

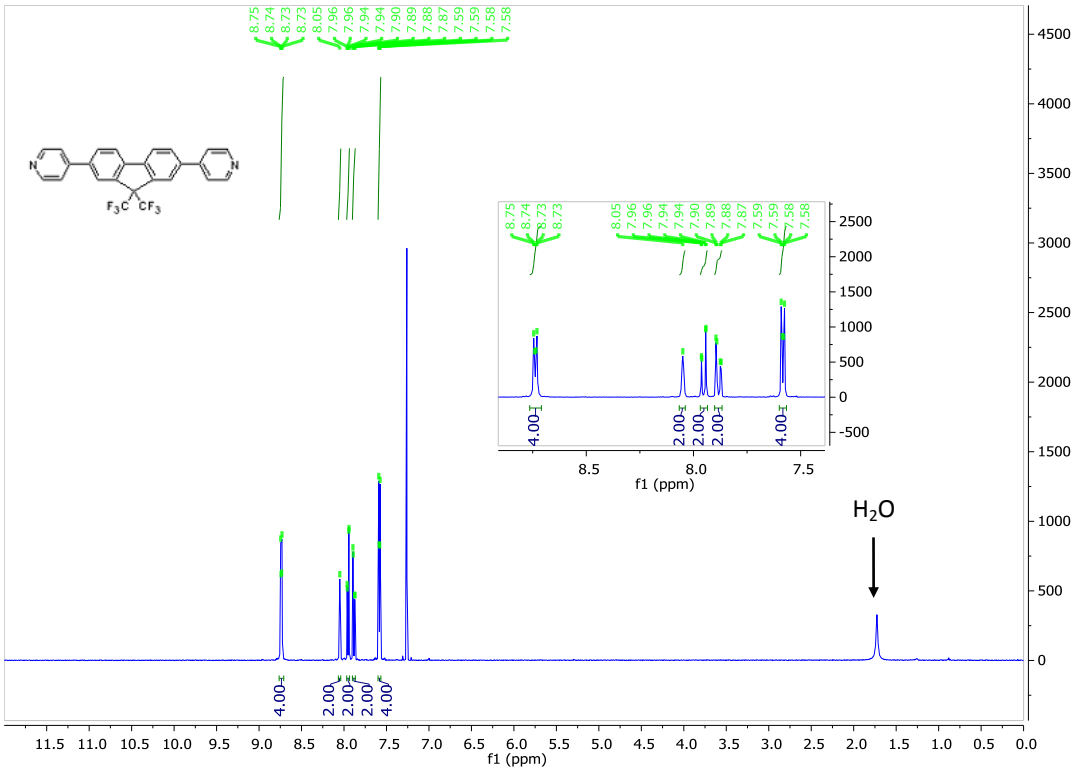

Figure S20. ^{1}H NMR spectrum of 2,7-dipyridinyl-9,9-bis(trifluoromethyl)fluorene **4**

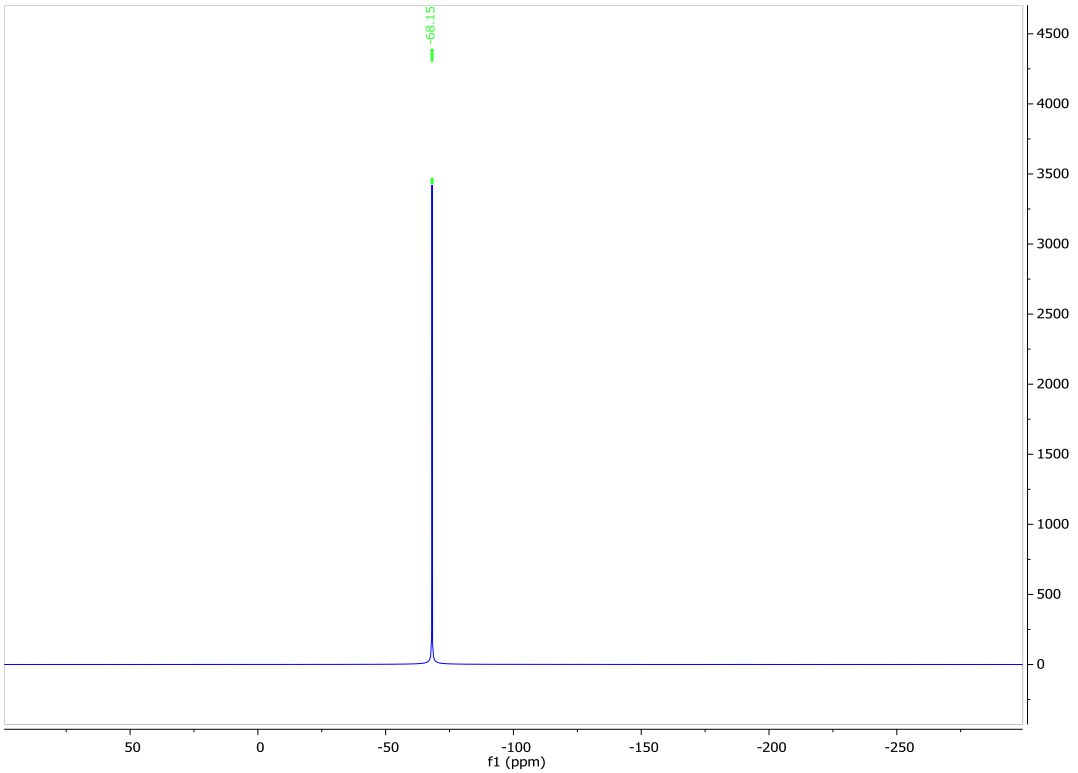

Figure S21. ^{19}F NMR spectrum of 2,7-dipyridinyl-9,9-bis(trifluoromethyl)fluorene **4**

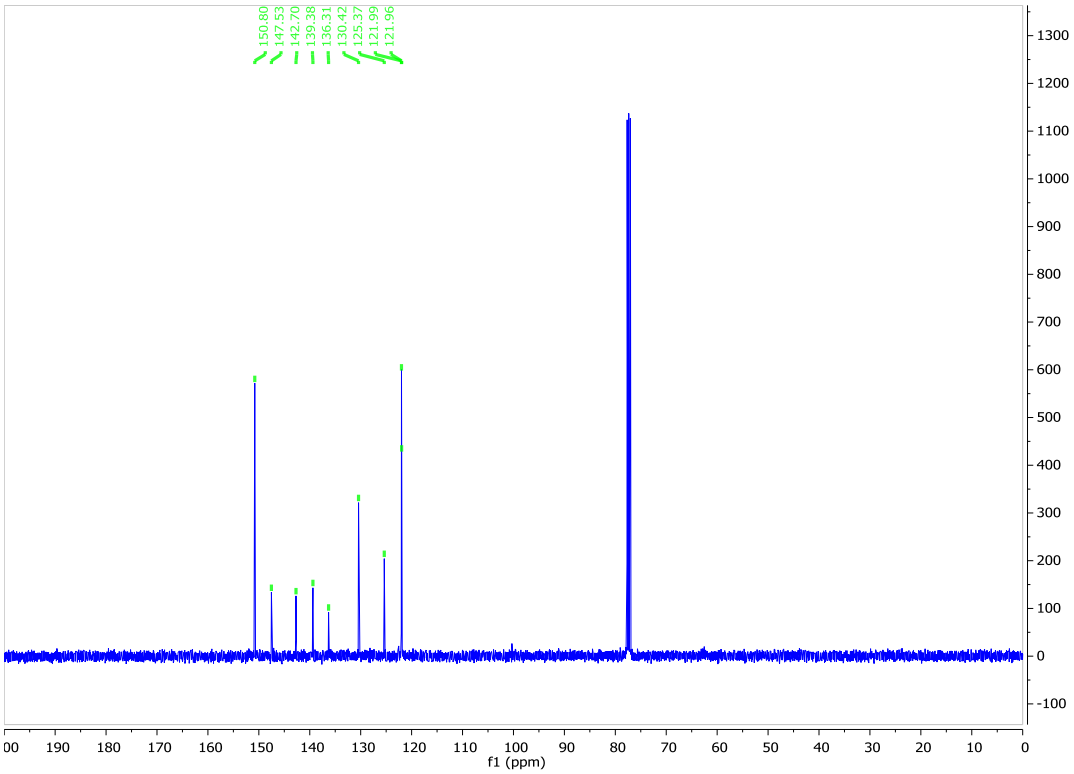

Figure S22. ^{13}C NMR spectrum of 2,7-dipyridinyl-9,9-bis(trifluoromethyl)fluorene **4**

e. Absorption and fluorescence spectra. The absorption and emission spectra of compounds **1**-**5** were recorded in dichloromethane solution at room temperature. The spectra are shown in Figure S23 and their wavelengths are summarized in Table S2. The spectra are characteristic of fluorene[4] and fluorenone[5] derivatives, with absorption in the ultraviolet region and emission in the blue region.

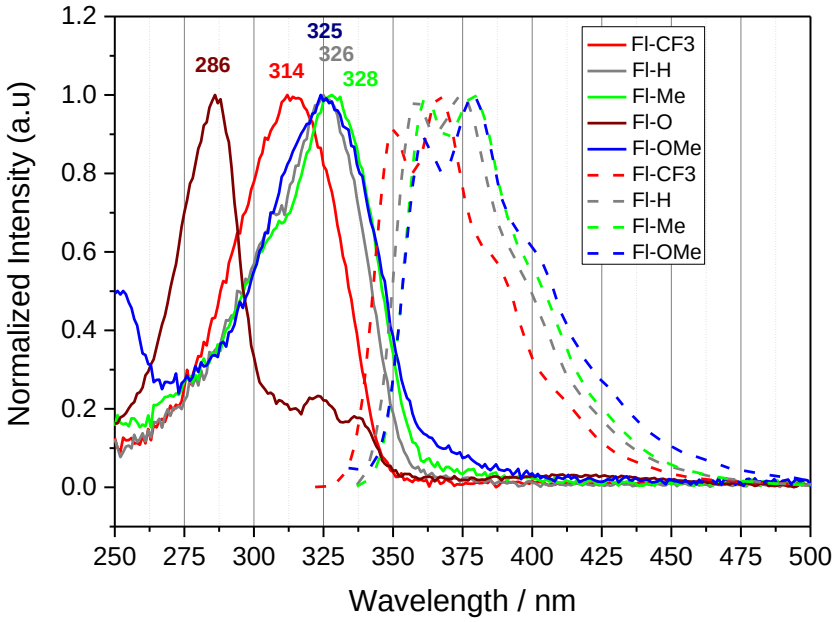

Figure S23. Normalized absorption (solid lines) and fluorescence (dashed lines) spectra.

Table S2. Absorption and fluorescence wavelengths recorded at room temperature in DCM.

Compound	Fl-H **1**	Fl-Me **2**	Fl-OMe **3**	Fl-CF_3 **4**	Fl-O **5**
λ_{max} abs (nm)	326	328	325	314	286, 323, 334
λ_{max} PL (nm)	358, 375, 400	361, 379, 402	361, 379, 403	351, 367, 387,414	Non-emissive

3. Conductance and thermopower measurements

a. Sample preparation

After annealing, the STM images of the gold substrate typically show clean surfaces with crystalline reconstruction of the gold surface and monoatomic steps (as shown in Figure S24), while G-Δz curves between the Au-Au electrodes show tunneling behavior in ambient conditions (see also ref. 10 in the manuscript).

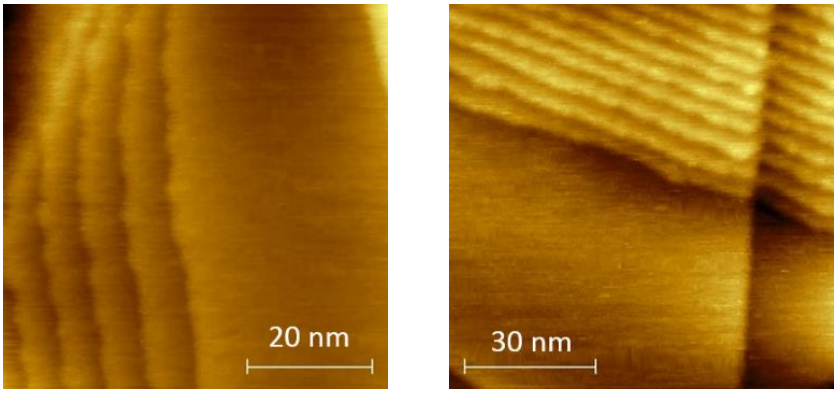

Figure S24. STM images of the Au substrate in ambient conditions.

b) Experimental techniques

Scanning tunneling microscopy (STM) measurements were performed using a home-built STM modified to measure simultaneously the conductance G and thermopower S of single-molecule junctions.[6] Mechanically cut Au tips (0.25 mm diameter, 99.99% purity, Goodfellow) were used to contact the molecules. STM-BJ measurements[6] were performed in ambient conditions and at room temperature, with a bias voltage V_{bias} of 200 mV applied to the substrate. Single-molecule junctions were formed after breaking the Au-Au contact formed by indenting the substrate with the STM tip. A 12 MΩ resistor in series with the tip-sample junction was used in order to monitor the Au-Au one-atom contact. Amplification of the current was performed using a double-stage, home-made, linear current-voltage (I-V)-converter with an overall gain of $2.6 \cdot 10^{10}$ V/A.

A 1 kΩ resistor mounted in the tip support was used as a heater to establish a temperature difference ΔT between the substrate (at room temperature, T_c) and the tip (heated at a temperature $T_h > T_c$). Thermoelectric properties of each molecule were measured by applying four different ΔTs, namely $\Delta T = T_h - T_c = 0\,K$, $\sim 15\,K$, $\sim 22\,K$ and $\sim 30\,K$, monitored with thermocouples in the resistor and substrate. For each ΔT, the system was allowed to stabilize for approximately 20 min before measurements were taken.

A thermovoltage V_{th} is generated in the junction as a consequence of the temperature difference applied. V_{th} consists of a contribution from the molecular junction $S\Delta T$ and a contribution from the tip-connecting lead $S_{lead}(-\Delta T)$, where S_{lead} is the thermopower of the lead. The current between the tip and substrate is given by

$$I = G(V_{bias} - V_{th}) = G(V_{bias} + S_{lead}\Delta T - S\Delta T) \qquad \text{(S2)}$$

where G is the conductance of the junction (Figure S25). Taking into account that for $V_{bias} = V_{th}$ the current vanishes, by measuring a current-voltage (I-V) curve the thermopower and

the conductance can be simultaneously obtained: the zero crossing yields V_{th} (and hence S) and the slope gives G.

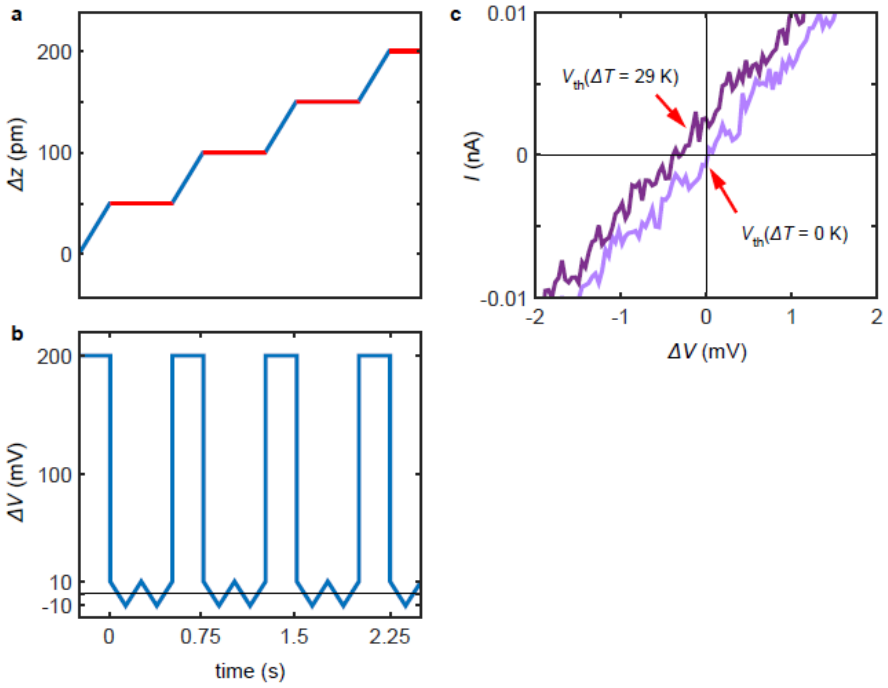

Figure S25. Experimental technique for the simultaneous measurement of conductance and thermopower. a,b) Tip displacement Δz and applied bias voltage ΔV at the molecular junction, respectively, as a function of time. The bias voltage is maintained at a fixed value V_{bias} during the tip motion (in blue in a) and every few picometers it is swept twice between $\pm\Delta V_0$ while the tip is stationary (in red in a). In the experiments, the bias voltage V_{bias} was set to 200 mV, ΔV_0 was set to 10 mV and the tip was stopped every 40-60 pm. c) Experimental *I-V* curves showing the voltage offset due to the temperature difference.

The thermopower S of single-molecule junctions was measured during the breaking of the junction, stopping the tip motion every 40-60 pm, as depicted in Figure S25. The bias voltage was maintained at a fixed value $\Delta V = V_{bias} = 200$ mV during the tip motion and it was swept twice every few picometers between $\pm\Delta V_0 = \pm 10$ mV while the tip is stationary. I-V curves show a voltage offset when measuring in the presence of a temperature difference ΔT between the two Au electrodes. This voltage offset corresponds to the thermovoltage V_{th} of the junction (once the electrical offsets are taken into account). Experiments were performed at zero ΔT and at three different ΔT values for each molecule to ensure a good linear fit of all the V_{th} values. By fitting the peak of the thermovoltage histograms of V_{th} at each ΔT to Gaussian distributions, from the mean value of the fit the most probable values $\overline{V_{th}}$ of the

single-molecule junctions are determined at each temperature and its standard deviation $\sigma_{V_{th}}$. The conductance is measured both from the current values while moving the tip ($V_{bias} =$ 200 mV) and from the slope of the *I-V* curves.

c) Conductance *G* and thermopower *S vs.* tip displacement Δz

After breaking the Au-Au contact, a molecular junction connecting a single molecule between both electrodes may be formed (which shows a plateau in the G-Δz curve) (see Figure S26) or, indeed, the tip may retract without connecting any molecule and hence, no plateau is observed. Table S3 gives the value of the ratio of the curves with plateau to overall acquired curves for each molecule.

Table S3. Percentage of G-Δz curves showing a plateau.

Molecule	Ratio
1 Fl-H	48%
2 Fl-Me	54%
3 Fl-OMe	77%
4 Fl-CF_3	71%
5 Fl-O	55%

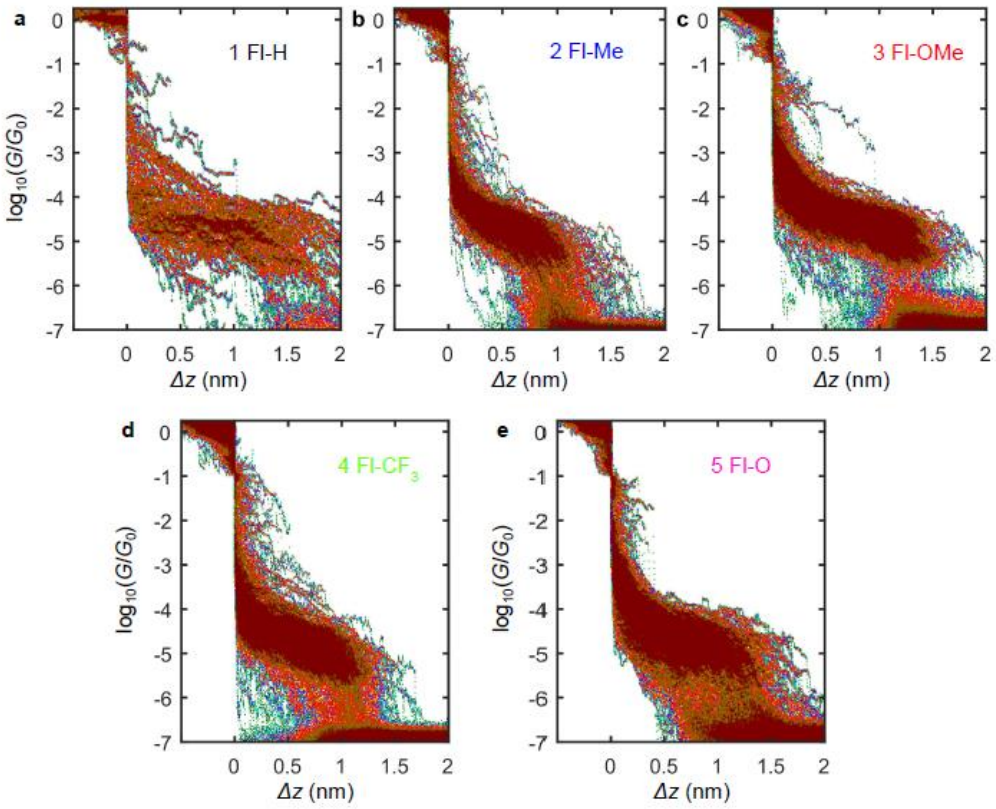

Figure S26. Conductance G vs. tip displacement Δz 2D histograms. The zero displacement was chosen to be the position where $G = 0.1\ G_0$.

The thermovoltage measured on the conductance plateau does not show any dependence on tip displacement as can be seen in Figures S27 and S28, corresponding to molecule **3** at a temperature difference of ΔT = 0 K and 22 K, respectively.

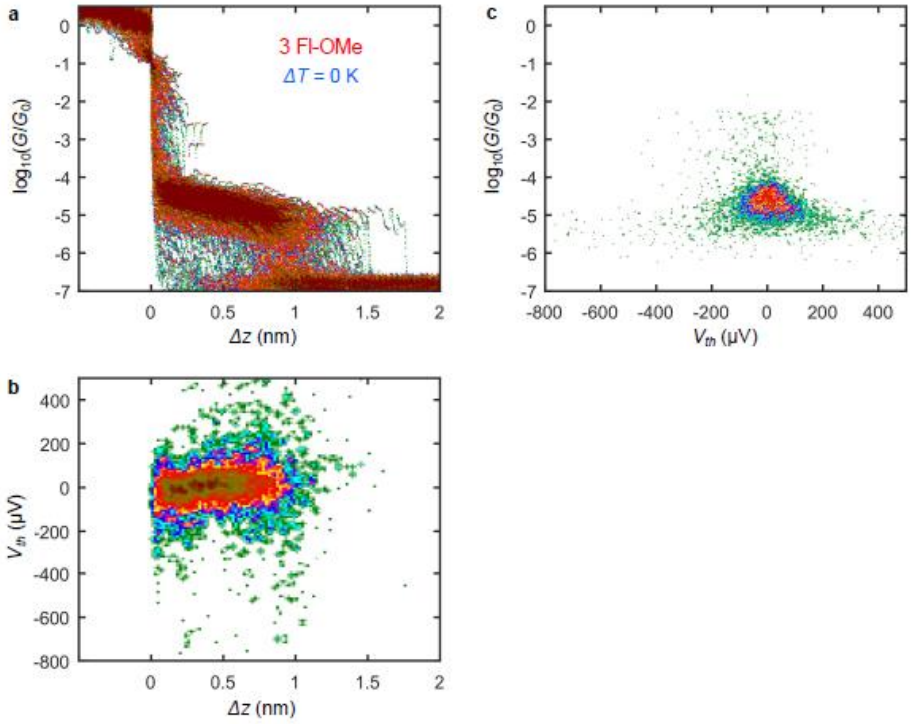

Figure S27. 2D histograms for molecule **3** when $\Delta T = 0\,K$. a) Conductance G vs. tip displacement Δz 2D histogram. The zero displacement was chosen to be the position where $G = 0.1\,G_0$. b) Thermovoltage V_{th} vs. tip displacement Δz 2D histogram. c) Conductance G vs. thermovoltage V_{th} 2D histogram.

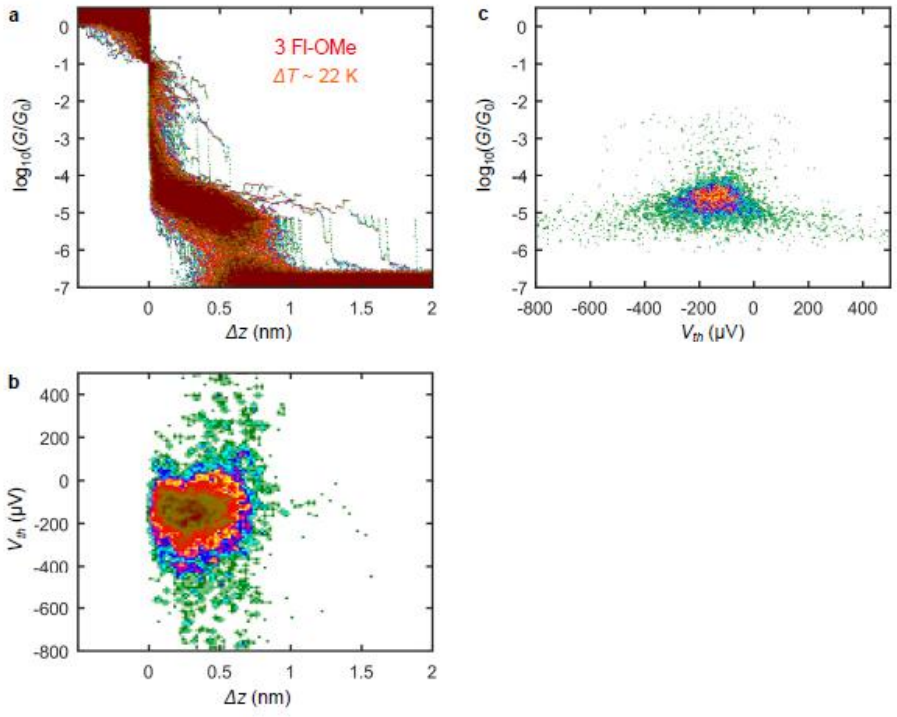

Figure S28. 2D histograms for molecule **3** when $\Delta T \sim 22\ K$. a) Conductance G vs. tip displacement Δz 2D histogram. The zero displacement was chosen to be the position where $G = 0.1\ G_0$. b) Thermovoltage V_{th} vs. tip displacement Δz 2D histogram. c) Conductance G vs. thermovoltage V_{th} 2D histogram.

4. References

1) Gantenbein, M.; Wang, L.; Al-jobory, A. A.; Ismael, A. K.; Lambert, C. J., Hong, W.; Bryce, M. R. Quantum interference and heteroaromaticity of para-and meta-linked bridged biphenyl units in single molecular conductance measurements. *Scientific Reports*, **2017**, *7*, 1794.

2) Blaazer, A. R.; Lange, J. H. M.; van der Neut, M. A. W.; Mulder, A.; den Boon, F. S.; Werkman, T. R.; Kruse, C. G.; Wadman, W. J. Novel Indole and Azaindole (Pyrrolopyridine) Cannabinoid (CB) Receptor Agonists: Design, Synthesis, Structure–activity Relationships, Physicochemical Properties and Biological Activity. *Eur. J. Med. Chem.* **2011**, *46*, 5086–5098.

3) Amara, J. P.; Swager, T. M. Conjugated Polymers with Geminal Trifluoromethyl Substituents Derived from Hexafluoroacetone. *Macromolecules* **2006**, *39*, 5753–5759.

4) Dias, F. B.; Pollock, S.; Hedley, G.; Pålsson, L-O.; Monkman, A.; Perepichka, I. I.; Igor F. Perepichka, I. F.; Tavasli, M.; Bryce, M. R. Intramolecular Charge Transfer Assisted by Conformational Changes in the Excited State of Fluorene-dibenzothiophene-*S,S*-dioxide Co-oligomers. *J. Phys. Chem. B* **2006**, *110*, 19329–19339.

5) Kukhta, N. A.; da Silva Filho, D. A.; Volyniuk, D.; Grazulevicius, J. V.; Sini, G. Can Fluorenone-Based Compounds Emit in the Blue Region? Impact of the Conjugation Length and the Ground-State Aggregation. *Chem. Mater*. **2017**, *29*, 1695–1707.

6) Evangeli, C.; Gillemot, K.; Leary, E.; González, M. T.; Rubio-Bollinger, G.; Lambert, C. J.; Agraït, N. Engineering the Thermopower of C_{60} Molecular Junctions. *Nano Lett.* **2013**, *13*, 2141−2145.